CHAPTER 3

# SOME INVESTIGATIONS ON MOORE-GIBSON-THOMPSON THERMOELASTICITY THEORY

## 3.1 On Propagation of Harmonic Plane Waves under the Moore-Gibson-Thompson Thermoelasticity Theory

### 3.1.1 Introduction[1]

In the previous chapter, some theoretical results have been established for the Moore-Gibson-Thompson (MGT) thermoelasticity theory. It has been observed that the domain of influence due to thermomechanical disturbance with bounded support is finite, if MGT thermoelasticity theory is employed instead of classical thermoelasticity theory. The current chapter further attempts to investigate some problems in the context of MGT thermoelasticity theory in order to better elaborate the understanding about this theory. This chapter is divided into two subchapters. The present subchapter examines the plane wave propagation under the MGT thermoelasticity theory.

Analysis of plane wave and its wave characterizations help in understanding the in-

[1]The content of this sub chapter is published in ***Waves in Random and Complex Media*** 1-24 (2021)

ternal structure of the material. Also, investigation of waves traveling through Earth is essential to get the information of Earth's internal structure; hence, the study of waves has useful applications in geophysics, mining, and seismology. Moreover, it must be mentioned here that such study of plane wave propagation in a thermoelastic medium is a topic of great concern of researchers because of its several applications in aeronautics, atomic physics, soil dynamics, thermal power plants, etc. Lessen (1957), Deresiewicz (1957), Chadwick and Sneddon (1958), and Chadwick (1960) are the pioneer researchers who examined the plane wave propagation in the classical thermoelasticity theory. The harmonic plane wave in the context of LS thermoelasticity theory was first studied by Nayfeh and Nemat-Nasser (1971). Puri (1972) re-examined plane wave propagation under the classical thermoelasticity theory. Further, Puri (1973) also discussed plane wave propagation under the LS thermoelastic model. The Whitham stability of thermoelastic plane waves under the LS thermoelasticity theory was established by Beevers (1973). In the context of GL model, the propagation and Whitham stability of harmonically time-dependent thermoelastic plane waves was investigated by Agarwal (1979). Haddow and Wegner (1996) re-investigated the plane wave propagation in view of the CTE, LS, and GL theories. Chandrasekharaiah (1996b) carried out the analysis of plane wave propagation under the GN-II model. Further, the plane wave propagation under the GN-III model was analyzed by Puri and Jordan (2004) and later on by Kothari and Mukhopadhyay (2012).

The main motive of the present subchapter is to investigate the propagation of plane harmonic waves under the MGT thermoelasticity theory. An isotropic, unbounded, and homogeneous thermoelastic medium is considered and the nature of harmonic plane wave propagating through the medium is studied. It is aimed to compare the results of plane waves in the MGT model with the corresponding results predicted by other existing theories. Therefore, this problem is studied with the unified governing equations of four different models, namely MGT, LS, GN-III, and Biot models. The work is

arranged in the following way. In Subsection 3.1.2, the basic governing equations under the above thermoelasticity theories are formulated and the dimensionless form of these equations is presented in a unified way. In Subsection 3.1.3, the dispersion relation is derived for longitudinal plane wave. The transverse wave is found to be unaffected due to thermal field, whereas the longitudinal wave is coupled with thermal wave. Hence, attention has been paid to the propagation of longitudinal mode wave. Two different modes of longitudinal wave, i.e. elastic and thermal mode waves are identified. The expressions of attenuation coefficient and wave number for elastic and thermal modes of longitudinal wave are obtained. Subsection 3.1.4 is devoted in finding analytical solutions of the dispersion relation in the cases of high frequency and low frequency values. In Subsection 3.1.5, the asymptotic results of various qualitative characterizations of the wave field such as phase velocity, specific loss, and penetration depth are derived for the MGT model. Next, the Whitham stability of plane waves under the MGT model is established in Subsection 3.1.6. Further, the computational work of the above-mentioned wave characteristics for intermediate values of frequency is carried out for all models as mentioned above. The numerical results in the present case are found to be in perfect match with the analytical findings. In Subection 3.1.7, numerical results are displayed through various graphs and discussed in a detailed way. Lastly, in Subsection 3.1.8, the important outcomes of the investigation in this subchapter are highlighted.

### 3.1.2 Basic Equations and Problem Formulation

An isotropic, unbounded, and homogeneous thermoelastic medium is considered. In order to analyze the propagation of harmonic plane waves under the MGT theory of thermoelasticity, the displacement equation of motion and the heat conduction equation in the absence of body forces and heat sources are presented as follows:

**Displacement equation of motion:**

$$\mu u_{i,jj} + (\lambda + \mu) u_{j,ji} - \gamma \theta_{,i} = \rho \ddot{u}_i. \tag{3.1.1}$$

**Heat conduction equation:**

$$\left(K^* + K\frac{\partial}{\partial t}\right)\nabla^2\theta = \left(\frac{\partial}{\partial t} + \tau_q \frac{\partial^2}{\partial t^2}\right)\left(\gamma T_0 \dot{u}_{i,i} + \rho C_E \dot{\theta}\right). \tag{3.1.2}$$

From the above set of Eqs. (3.1.1) and (3.1.2), the respective system under four different theories of thermoelasticity can be extracted as special cases of the present model by setting the parameter values as follows:

- Biot classical model: $K^* = \tau_q = 0$.
- LS model: $K^* = 0$.
- GN-III model: $\tau_q = 0$.

Hence, for MGT model: $K^* \neq 0$, $\tau_q \neq 0$.

For the sake of simplification of Eqs. (3.1.1) and (3.1.2), the following dimensionless transformations are introduced:

$$u_i' = \frac{u_i}{c_0 t_0}, \;\; x_i' = \frac{x_i}{c_0 t_0}, \;\; t' = \frac{t}{t_0}, \;\; \theta' = \frac{\theta}{T_0}, \;\; \tau_q' = \frac{\tau_q}{t_0},$$

where $c_0 = \sqrt{\frac{(\lambda+2\mu)}{\rho}}$ is the velocity of predominantly elastic waves and $t_0 (> 0)$ is the time of characteristic response for the medium.

Using the above dimensionless variables and parameters, Eqs. (3.1.1) and (3.1.2) reduce

to the following forms after dropping all the primes for simplicity:

$$\mu u_{i,jj} + (\lambda + \mu) u_{j,ji} - \gamma T_0 \theta_{,i} = \rho c_0^2 \ddot{u}_i, \tag{3.1.3}$$

$$\left(k_2 + k_1 \frac{\partial}{\partial t}\right) \nabla^2 \theta = \left(\frac{\partial}{\partial t} + \tau_q \frac{\partial^2}{\partial t^2}\right) \left(a_2 \dot{u}_{i,i} + \dot{\theta}\right), \tag{3.1.4}$$

where the non-dimensional notations are employed as follows:

$$k_1 = \frac{K}{\rho C_E c_0^2 t_0}, \quad k_2 = \frac{K^*}{\rho C_E c_0^2}, \quad a_2 = \frac{\gamma}{\rho C_E}.$$

### 3.1.3 Harmonic Plane Waves

It is observed that the transverse wave is not modified by, nor contributed to, the temperature field of the medium. However, the longitudinal wave is found to be coupled with thermal and mechanical fields. For this reason, we turn our attention on the longitudinal plane wave instead of the transverse wave in the present context. The solutions of the longitudinal plane wave are considered as follows:

$$u_j = \mathfrak{A} d_j \exp\left[\mathrm{i}\left(\omega t - \Upsilon n_i x_i\right)\right], \tag{3.1.5}$$

$$\theta = \mathfrak{B} \exp\left[\mathrm{i}\left(\omega t - \Upsilon n_i x_i\right)\right], \tag{3.1.6}$$

where $\Upsilon$ is the complex wave number, $\mathfrak{A}$ and $\mathfrak{B}$ denote the amplitudes of wave and $\omega(>0)$ denotes the non-dimensional angular frequency of the wave. Here $d_j$ represents the component of unit vector in the direction of the displacement, $x_i$ denotes the component of the position vector and $n_j$ represents the component of unit vector normal to the wavefront. $\mathrm{Re}[\Upsilon] > 0$ and $\mathrm{Im}[\Upsilon] \leq 0$ are considered for physically realistic behavior of wave. Further, $\frac{\omega}{\mathrm{Re}(\Upsilon)}$ denotes the phase velocity of wave, which is analogous to the longitudinal wave where frequency is denoted by $\frac{\omega}{2\pi}$ and wavelength is denoted by $\frac{2\pi}{\mathrm{Re}(\Upsilon)}$.

#### 3.1.3.1 Dispersion relation and its derivation

Now, substituting Eqs. (3.1.5) and (3.1.6) into Eqs. (3.1.3) and (3.1.4), the following system of equations are acquired after mathematical manipulations and simplifications:

$$\left(\Upsilon^2-\omega^2\right)\mathfrak{A}-\mathrm{i}\ a_1\Upsilon\mathfrak{B}=0, \tag{3.1.7}$$

$$\left(\mathrm{i}a_2\Upsilon\omega^2-a_2\tau_q\Upsilon\omega^3\right)\mathfrak{A}+\left[\mathrm{i}\left(k_1\omega\Upsilon^2-\tau_q\omega^3\right)+k_2\Upsilon^2-\omega^2\right]\mathfrak{B}=0, \tag{3.1.8}$$

where $a_1=\frac{\gamma T_0}{\lambda+2\mu}$ and the property $d_jn_j=n_jn_j=1$ is used.

In order to obtain the non-trivial solution of this system of Eqs. (3.1.7) and (3.1.8), the determinant of the coefficient matrix in this homogeneous system will be zero, i.e.,

$$\begin{vmatrix} \Upsilon^2-\omega^2 & -\mathrm{i}\ a_1\Upsilon \\ \mathrm{i}a_2\Upsilon\omega^2-a_2\tau_q\Upsilon\omega^3 & \mathrm{i}\left(k_1\omega\Upsilon^2-\tau_q\omega^3\right)+k_2\Upsilon^2-\omega^2 \end{vmatrix}=0$$

which yields the bi-quadratic dispersion relation as follows:

$$\Upsilon^4\left[k_2+\mathrm{i}k_1\omega\right]-\Upsilon^2\left[\omega^2+k_2\omega^2+a_1a_2\omega^2+\mathrm{i}\left(k_1\omega^3+\tau_q\omega^3+a_1a_2\tau_q\omega^3\right)\right] +\omega^4+\mathrm{i}\tau_q\omega^5=0. \tag{3.1.9}$$

Further, for simplicity of this dispersion relation (3.1.9), we multiply this equation throughout by $k_2-\mathrm{i}k_1\omega$ and make the coefficient of $\Upsilon^4$ real. Finally, the following simplified dispersion relation is achieved in terms of four models:

$$B(\omega)\Upsilon^4-(G-\mathrm{i}L)\,\Upsilon^2+(M-\mathrm{i}N)=0, \tag{3.1.10}$$

where

$$B(\omega) = b_1\omega^2 + b_2, \quad G = f_1\omega^4 + f_2\omega^2, \quad L = g_1\omega^3,$$
$$M = l_1\omega^6 + l_2\omega^4, \quad N = m_1\omega^5,$$

and

$$b_1 = k_1^2, \quad b_2 = k_2^2, \quad f_1 = k_1 h\tau_q + k_1^2, \quad f_2 = k_2 h + k_2^2,$$
$$g_1 = k_1 h - k_2\tau_q h, \quad l_1 = k_1\tau_q, \quad l_2 = k_2, \quad m_1 = k_1 - k_2\tau_q,$$
$$h = 1 + \varepsilon, \quad \varepsilon = a_1 a_2.$$

Eq. (3.1.10) expresses the dispersion relation in view of the MGT model where $K^* \neq 0$ and $\tau_q \neq 0$. Therefore, it is easy to observe that the dispersion relation for other three different models can be obtained from the dispersion relation given by Eq. (3.1.10) as following particular cases:

- Biot model ($K^* = \tau_q = 0$)

$$k_1\Upsilon^4 + \left[-k_1\omega^2 + \mathrm{i}(1+\varepsilon)\omega\right]\Upsilon^2 - \mathrm{i}\omega^3 = 0. \tag{3.1.11}$$

- LS model ($K^* = 0$)

$$k_1\Upsilon^4 + \left[\omega\left(1+\varepsilon\right)\left(\mathrm{i} - \tau_q\omega\right) - k_1\omega^2\right]\Upsilon^2 - \omega^3\left(\mathrm{i} - \tau_q\omega\right) = 0. \tag{3.1.12}$$

- GN-III model ($\tau_q = 0$)

$$\left(k_1^2\omega^2 + k_2^2\right)\Upsilon^4 - \left[k_1^2\omega^4 + \left(k_2(1+\varepsilon) + k_2^2\right)\omega^2 - \mathrm{i}k_1(1+\varepsilon)\omega^3\right]\Upsilon^2 + k_2\omega^4 - \mathrm{i}k_1\omega^5 = 0. \tag{3.1.13}$$

Hence, the dispersion relation in view of the MGT model is a fusion of dispersion

relations for the above-mentioned models. Further, the dispersion relation given by Eq. (3.1.11) is similar to the dispersion relation as shown by Chadwick and Sneddon (1958) for the classical thermoelastic model and the dispersion relation given by Eq. (3.1.12) corresponds to the dispersion relation derived by Puri (1973) for the case of LS model. Moreover, the dispersion relation given by Eq. (3.1.13) completely matches with the dispersion relation as derived by Puri and Jordan (2004) for the GN-III model.

#### 3.1.3.2 Expressions for attenuation coefficient and wave number

The wave number and attenuation coefficient are represented by $\Upsilon$ and the absolute value of $\mathrm{Im}[\Upsilon]$, respectively. Since the dispersion relation under the MGT model is represented by Eq. (3.1.10), therefore, this equation is solved as quadratic in $\Upsilon^2$. If $\pm\Upsilon_1$ and $\pm\Upsilon_2$ are the roots of Eq. (3.1.10), then we have

$$\Upsilon_{1,2}^2 = \frac{(G - \mathrm{i}L) \pm \sqrt{A(\omega)}}{2B(\omega)}, \tag{3.1.14}$$

where

$$\begin{aligned} \mathrm{Real}(A(\omega)) &= P_1\omega^8 + P_2\omega^6 + P_3\omega^4, \\ \mathrm{Im}(A(\omega)) &= Q_1\omega^7 + Q_2\omega^5, \end{aligned}$$

and

$$\begin{aligned} P_1 &= f_1^2 - 4b_1l_1, \\ P_2 &= 2f_1f_2 - g_1^2 - 4b_1l_2 - 4b_2l_1, \\ P_3 &= f_2^2 - 4b_2l_2, \\ Q_1 &= -2f_1g_1 + 4b_1m_1, \\ Q_2 &= -2f_2g_1 + 4b_2m_1. \end{aligned}$$

To solve Eq. (3.1.14), a standard theorem of complex analysis (Ponnusamy (2005)) is used which is as follows:

**Theorem** (Ponnusamy (2005)). If $z = x + \mathrm{i}y \in \mathbb{C}$ and $w^2 = z$, then values of $w$ are given as

$$w = \pm \left[ \sqrt{\frac{x + \sqrt{x^2 + y^2}}{2}} + \mathrm{i}\,\mathrm{sgn}(y) \sqrt{\frac{-x + \sqrt{x^2 + y^2}}{2}} \right], \tag{3.1.15}$$

where

$$\mathrm{sgn}(y) = \begin{cases} +1 & \text{if } y \geq 0 \\ -1 & \text{if } y < 0 \end{cases}.$$

Now, out of the four roots of Eq. (3.1.14), we are only interested in two roots whose imaginary parts are negative. These two roots for $\Upsilon$ identify that the longitudinal wave propagating through the medium is a composition of two coupled waves. Now, these two roots with negative imaginary parts are denoted by $\Upsilon_{1,2}$ and it is to be mentioned that $\Upsilon_1$ and $\Upsilon_2$ are analogous to two modes of the longitudinal wave where we consider that $\Upsilon_1$ corresponds to predominantly elastic wave which is also represented by $\Upsilon_E$ and $\Upsilon_2$ corresponds to predominantly thermal wave which is represented by $\Upsilon_T$. The analytical expressions for these two values of $\Upsilon$ are derived by using the above-mentioned result given by Eq. (3.1.15).

### 3.1.4 Analytical Results

To examine the plane wave propagation under the MGT thermoelasticity theory, we analyze the results of longitudinal plane waves as described above. In this subsection, specifically, we concentrate on the limiting behavior of elastic as well as thermal mode waves for the cases of very high-frequency and very low-frequency values. Therefore,

first of all, the high and low-frequency asymptotic expressions for $\Upsilon_{1,2}$ are derived from Eq. (3.1.14) with the help of above theorem in cases: $\omega \to \infty$ and $\omega \to 0$, respectively.

#### 3.1.4.1 High-frequency asymptotic expressions

In order to obtain the high frequency ($\omega >>> 1$) asymptotic expressions, Eq. (3.1.14) is expanded in terms of large $\omega$ and higher powers of $1/\omega$ are neglected, then Eq. (3.1.14) yields

$$\Upsilon_{1,2}^2 = \frac{(G - \mathrm{i}L) \pm (C + \mathrm{i}D)}{2B(\omega)},$$

where

$$C = \sqrt{P_1}\omega^4 + \left(\frac{P_2}{2\sqrt{P_1}} + \frac{Q_1^2}{8P_1^{3/2}}\right)\omega^2 + \left(\frac{P_3}{2\sqrt{P_1}} - \frac{P_2^2}{8p_1^{3/2}} + \frac{Q_1Q_2}{4P_1^{3/2}} - \frac{3Q_1^2P_2}{16P_1^{5/2}}\right) + O\left(\frac{1}{\omega^2}\right)$$

and

$$D = \frac{Q_1}{2\sqrt{P_1}}\omega^3 + \left(\frac{Q_2}{2\sqrt{P_1}} - \frac{P_2Q_1}{4P_1^{3/2}} - \frac{Q_1^3}{16P_1^{5/2}}\right)\omega + \left(-\frac{P_2Q_2}{4P_1^{3/2}} - \frac{P_3Q_1}{4P_1^{3/2}} - \frac{3Q_1^2Q_2}{16P_1^{5/2}} + \frac{3P_2^2Q_1}{16P_1^{5/2}}\right)\frac{1}{\omega} + O\left(\frac{1}{\omega^3}\right).$$

**Analytical results for $\Upsilon_{1,2}$** (i.e., $\Upsilon_{E,T}$):

We expand the equation for $\Upsilon_{1,2}^2$ in terms of large $\omega$ and neglect higher powers of $1/\omega$. Now, making use of the theorem as discussed in subsection 3.1.3 and after some manipulations, the following asymptotic expressions for the roots of Eq. (3.1.14) is achieved:

$$\Upsilon_1 \approx \sqrt{R_1}\omega\left(1+\frac{4R_1R_2+S_1^2}{8R_1^2}\frac{1}{\omega^2}\right)-\frac{\mathrm{i}}{2}\frac{S_1}{\sqrt{R_1}}\left(1+\frac{8S_2R_1^2-4R_1R_2S_1-S_1^3}{8S_1R_1^2}\frac{1}{\omega^2}\right)(\omega\to\infty), \tag{3.1.16}$$

$$\Upsilon_2 \approx \sqrt{T_1}\omega\left(1+\frac{4T_1T_2+U_1^2}{8T_1^2}\frac{1}{\omega^2}\right)-\frac{\mathrm{i}}{2}\frac{U_1}{\sqrt{T_1}}\left(1+\frac{8U_2T_1^2-4T_1T_2U_1-U_1^3}{8U_1T_1^2}\frac{1}{\omega^2}\right)(\omega\to\infty), \tag{3.1.17}$$

where

$$\begin{aligned}
R_1 &= \frac{f_1+\sqrt{P_1}}{2b_1},\\
R_2 &= \frac{1}{2b_1^2}\left[-\left(\sqrt{P_1}+f_1\right)b_2+\left(\frac{4P_1P_2+Q_1^2}{8P_1^{3/2}}+f_2\right)b_1\right],\\
S_1 &= \frac{1}{4b_1}\left(2g_1-\frac{Q_1}{\sqrt{P_1}}\right),\\
S_2 &= \frac{1}{32b_1^2}\left[8\left(2g_1-\frac{Q_1}{\sqrt{P_1}}\right)b_2+\left(\frac{Q_1^3+4P_2Q_1P_1-8Q_2P_1^2}{P_1^{5/2}}\right)b_1\right],\\
T_1 &= \frac{f_1-\sqrt{P_1}}{2b_1},\\
T_2 &= \frac{1}{2b_1^2}\left[-\left(f_1-\sqrt{P_1}\right)b_2+\left(f_2-\frac{4P_1P_2+Q_1^2}{8P_1^{3/2}}\right)b_1\right],\\
U_1 &= \frac{1}{4b_1}\left(2g_1+\frac{Q_1}{\sqrt{P_1}}\right),\\
U_2 &= \frac{1}{32b_1^2}\left[-8\left(2g_1+\frac{Q_1}{\sqrt{P_1}}\right)b_2+\left(\frac{8Q_2P_1^2-Q_1^3-4P_2Q_1P_1}{P_1^{5/2}}\right)b_1\right].
\end{aligned}$$

#### 3.1.4.2 Low-frequency asymptotic expressions

In this case, we expand Eq. (3.1.14) for very very small $\omega$ ($\omega << 1$) and employ the same method as discussed above, then Eq. (3.1.14) yields

$$\Upsilon_{1,2}^2 = \frac{(G-\mathrm{i}L)\pm(C'+\mathrm{i}D')}{2B(\omega)},$$

where

$$C' = \sqrt{P_3}\omega^2 + \left(\frac{P_2}{2\sqrt{P_3}} + \frac{Q_2^2}{8P_3^{3/2}}\right)\omega^4 + O\left(\omega^6\right),$$
$$D' = \frac{Q_2}{2\sqrt{P_3}}\omega^3 + \left(\frac{Q_1}{2\sqrt{P_3}} - \frac{P_2Q_2}{4P_3^{3/2}} - \frac{Q_2^3}{16P_3^{5/2}}\right)\omega^5 + O\left(\omega^7\right).$$

**Analytical results for $\Upsilon_{1,2}$:**

Equation for $\Upsilon_{1,2}^2$ is expanded in terms of very very small $\omega$. Now, making use of the theorem as discussed in subsection 3.1.3 and after some manipulations, the following asymptotic expressions for the roots of Eq. (3.1.14) is acquired:

$$\Upsilon_1 \approx \sqrt{W_1}\omega\left(1 + \frac{4W_1W_2 + X_1^2}{8W_1^2}\omega^2\right) - \frac{\mathrm{i}}{2}\frac{X_1}{\sqrt{W_1}}\omega^2\left(1 + \frac{8X_2W_1^2 - 4W_1W_2X_1 - X_1^3}{8X_1W_1^2}\omega^2\right)(\omega \to 0), \tag{3.1.18}$$

$$\Upsilon_2 \approx \sqrt{Y_1}\omega\left(1 + \frac{4Y_1Y_2 + Z_1^2}{8Y_1^2}\omega^2\right) - \frac{\mathrm{i}}{2}\frac{Z_1}{\sqrt{Y_1}}\omega^2\left(1 + \frac{8Z_2Y_1^2 - 4Y_1Y_2Z_1 - Z_1^3}{8Z_1Y_1^2}\omega^2\right)(\omega \to 0), \tag{3.1.19}$$

where

$$W_1 = \frac{f_2 + \sqrt{P_3}}{2b_2},$$
$$W_2 = \frac{1}{2b_2^2}\left[-\left(\sqrt{P_3} + f_2\right)b_1 + \left(\frac{4P_2P_3 + Q_2^2}{8P_3^{3/2}} + f_1\right)b_2\right],$$
$$X_1 = \frac{1}{4b_2}\left(2g_1 - \frac{Q_2}{\sqrt{P_3}}\right),$$
$$X_2 = \frac{1}{32b_2^2}\left[8\left(2g_1 - \frac{Q_2}{\sqrt{P_3}}\right)b_1 + \left(\frac{Q_2^3 + 4P_2Q_2P_3 - 8Q_1P_3^2}{P_3^{5/2}}\right)b_2\right],$$
$$Y_1 = \frac{f_2 - \sqrt{P_3}}{2b_2},$$
$$Y_2 = \frac{1}{2b_2^2}\left[-\left(f_2 - \sqrt{P_3}\right)b_1 + \left(f_1 - \frac{4P_2P_3 + Q_2^2}{8P_3^{3/2}}\right)b_2\right],$$

$$Z_1 = \frac{1}{4b_2}\left(2g_1 + \frac{Q_2}{\sqrt{P_3}}\right),$$
$$Z_2 = \frac{1}{32b_2^2}\left[-8\left(2g_1 + \frac{Q_2}{\sqrt{P_3}}\right)b_1 + \left(\frac{8Q_1P_3^2 - Q_2^3 - 4P_2Q_2P_3}{P_3^{5/2}}\right)b_2\right].$$

### 3.1.5 Asymptotic Results for Different Wave Fields

For the purpose of studying the detailed analysis of plane waves, the important wave components are discussed in this subsection. Particularly, the asymptotic expressions for the phase velocity, specific loss, and penetration depth for elastic mode wave and thermal mode wave are derived under the cases of high-frequency and low-frequency.

#### 3.1.5.1 Phase velocity

The phase velocity for waves is defined in the following way:

$$V_{E,T} = V_{1,2} = \frac{\omega}{\text{Real}\left(\Upsilon_{1,2}\right)}. \tag{3.1.20}$$

In the above formula, $V_E$ represents the phase velocity for elastic mode wave and $V_T$ represents the phase velocity for thermal mode wave.

Thus, employing the analytical results of $\Upsilon_{1,2}$ given by Eqs. (3.1.16) – (3.1.19) and applying formula given by Eq. (3.1.20), the following asymptotic results for $V_E$ and $V_T$ under the high-frequency and low-frequency cases are obtained:

- **Asymptotic expressions of phase velocity for high-frequency**

$$V_E \sim \frac{1}{\sqrt{R_1}}\left[1 - \frac{1}{8R_1^2}\left(4R_1R_2 + S_1^2\right)\frac{1}{\omega^2} + O\left(\frac{1}{\omega^4}\right)\right], \tag{3.1.21}$$
$$V_T \sim \frac{1}{\sqrt{T_1}}\left[1 - \frac{1}{8T_1^2}\left(4T_1T_2 + U_1^2\right)\frac{1}{\omega^2} + O\left(\frac{1}{\omega^4}\right)\right], \qquad \text{as } \omega \to \infty \tag{3.1.22}$$

- **Asymptotic expressions of phase velocity for low-frequency**

$$V_E \sim \frac{1}{\sqrt{W_1}}\left[1-\frac{1}{8W_1^2}\left(4W_1W_2+X_1^2\right)\omega^2+O\left(\omega^4\right)\right], \tag{3.1.23}$$

$$V_T \sim \frac{1}{\sqrt{Y_1}}\left[1-\frac{1}{8Y_1^2}\left(4Y_1Y_2+Z_1^2\right)\omega^2+O\left(\omega^4\right)\right], \qquad \text{as } \omega\to 0 \tag{3.1.24}$$

#### 3.1.5.2 Specific loss

The specific loss of wave is defined by

$$\mathrm{SP}_{E,T}=\mathrm{SP}_{1,2}=\left(\frac{\triangle W}{W}\right)_{E,T}=\left(\frac{\triangle W}{W}\right)_{1,2}=4\pi\frac{|\mathrm{Im}\left(\Upsilon_{1,2}\right)|}{|\mathrm{Real}\left(\Upsilon_{1,2}\right)|}, \tag{3.1.25}$$

where $\mathrm{SP}_E$ and $\mathrm{SP}_T$ represent the specific loss for elastic mode waves and thermal mode waves, respectively.

Now, using the analytical results of $\Upsilon_{1,2}$ given by Eqs. (3.1.16) – (3.1.19) and applying formula given by Eq. (3.1.25), the following asymptotic results for $\mathrm{SP}_E$ and $\mathrm{SP}_T$ under the high and low frequency cases are obtained:

- **Asymptotic expressions of specific loss for high-frequency**

$$\mathrm{SP}_E \sim \frac{2\pi S_1}{R_1}\frac{1}{\omega}\left[1+\frac{8S_2R_1^2-8R_1R_2S_1-2S_1^3}{8S_1R_1^2}\frac{1}{\omega^2}+O\left(\frac{1}{\omega^4}\right)\right], \tag{3.1.26}$$

$$\mathrm{SP}_T \sim \frac{2\pi U_1}{T_1}\frac{1}{\omega}\left[1+\frac{8U_2T_1^2-8T_1T_2U_1-2U_1^3}{8U_1T_1^2}\frac{1}{\omega^2}+O\left(\frac{1}{\omega^4}\right)\right], \qquad \text{as } \omega\to\infty \tag{3.1.27}$$

- **Asymptotic expressions of specific loss for Low-frequency**

$$\mathrm{SP}_E \sim \frac{2\pi X_1}{W_1}\omega\left[1+\frac{8X_2W_1^2-8W_1W_2X_1-2X_1^3}{8X_1W_1^2}\omega^2+O\left(\omega^4\right)\right], \tag{3.1.28}$$

$$\mathrm{SP}_T \sim \frac{2\pi Z_1}{Y_1}\omega\left[1+\frac{8Z_2Y_1^2-8Y_1Y_2Z_1-2Z_1^3}{8Z_1Y_1^2}\omega^2+O\left(\omega^4\right)\right], \qquad \text{as } \omega\to 0 \tag{3.1.29}$$

#### 3.1.5.3 Penetration depth

The penetration depth of wave is calculated by the following relation:

$$\delta_{E,T} = \delta_{1,2} = \frac{1}{|\mathrm{Im}\,(\Upsilon_{1,2})|}. \tag{3.1.30}$$

In the above relation, $\delta_E$ represents the penetration depth for elastic mode waves and $\delta_T$ represents the penetration depth for thermal mode waves.

Now, using the analytical results of $\Upsilon_{1,2}$ given by Eqs. (3.1.16) – (3.1.19) and applying formula given by Eq. (3.1.30), we obtain the following asymptotic results for $\delta_E$ and $\delta_T$ under the high-frequency and low-frequency cases:

- **Asymptotic expressions of penetration depth for high-frequency**

$$\delta_E \sim \frac{2\sqrt{R_1}}{S_1}\left(1 - \frac{8S_2R_1^2 - 4R_1R_2S_1 - S_1^3}{8S_1R_1^2}\frac{1}{\omega^2}\right), \tag{3.1.31}$$

$$\delta_T \sim \frac{2\sqrt{T_1}}{U_1}\left(1 - \frac{8U_2T_1^2 - 4T_1T_2U_1 - U_1^3}{8U_1T_1^2}\frac{1}{\omega^2}\right), \qquad \text{as} \quad \omega \to \infty \tag{3.1.32}$$

- **Asymptotic expressions of penetration depth for low-frequency**

$$\delta_E \sim \frac{2\sqrt{W_1}}{X_1}\frac{1}{\omega^2}\left(1 - \frac{8X_2W_1^2 - 4W_1W_2X_1 - X_1^3}{8X_1W_1^2}\omega^2\right), \tag{3.1.33}$$

$$\delta_T \sim \frac{2\sqrt{Y_1}}{Z_1}\frac{1}{\omega^2}\left(1 - \frac{8Z_2Y_1^2 - 4Y_1Y_2Z_1 - Z_1^3}{8Z_1Y_1^2}\omega^2\right), \qquad \text{as} \ \ \omega \to 0 \tag{3.1.34}$$

### 3.1.6 Stability Analysis

Before going to the main result, we discuss the method of stability analysis developed by Whitham (1974) which is known as Whitham's stability criterion. According to this criterion, this method can be applied to the partial differential equations that can be expressed as follows:

$$\left(\frac{\partial}{\partial t}+v_1\frac{\partial}{\partial x}\right)...\left(\frac{\partial}{\partial t}+v_l\frac{\partial}{\partial x}\right)\varphi+\zeta\left(\frac{\partial}{\partial t}+r_1\frac{\partial}{\partial x}\right)...\left(\frac{\partial}{\partial t}+r_m\frac{\partial}{\partial x}\right)\varphi=0, \quad (3.1.35)$$

where $l<m$ and $\zeta$ is real. If $l=m-1$ and $\zeta\geq 0$, and if the wave speeds $v_1, v_2, ..., v_l$ and $r_1, r_2, ..., r_m$ are distinct and real, then plane waves are stable from the Whitham's stability criterion, provided

$$r_1>v_1>r_2>v_2>...>v_{m-1}>r_m. \quad (3.1.36)$$

#### 3.1.6.1 Stability analysis of plane waves in the MGT model

Now, we will analyze the stability of plane waves under the MGT thermoelastic model on the basis of our obtained results. In order to establish the stability of plane waves, the Whitham's stability criteria as discussed above is applied.

To apply Whitham's stability criterion in the present context, it is considered that plane waves propagate along the $x$-axis. Therefore, for the case of one spatial dimension, Eqs. (3.1.3) and (3.1.4) can be rewritten as follows:

$$(2\mu+\lambda)\frac{\partial^2 u}{\partial x^2}-\gamma T_0\frac{\partial\theta}{\partial x}=\rho c_0^2\frac{\partial^2 u}{\partial t^2}, \quad (3.1.37)$$

$$\left(k_2+k_1\frac{\partial}{\partial t}\right)\frac{\partial^2\theta}{\partial x^2}=\left(\frac{\partial}{\partial t}+\tau_q\frac{\partial^2}{\partial t^2}\right)\left(a_2\frac{\partial^2 u}{\partial x\partial t}+\frac{\partial\theta}{\partial t}\right). \quad (3.1.38)$$

Elimination of $\theta$ from Eqs. (3.1.37) and (3.1.38) yields the following fifth-order PDE:

$$\left[\frac{\partial^4}{\partial t^4}-(k_2+1+\varepsilon)\frac{\partial^4}{\partial t^2\partial x^2}+k_2\frac{\partial^4}{\partial x^4}\right]u+\frac{\partial}{\partial t}\left[k_1\frac{\partial^4}{\partial x^4}-(k_1+\tau_q+\varepsilon\tau_q)\frac{\partial^4}{\partial x^2\partial t^2}+\tau_q\frac{\partial^4}{\partial t^4}\right]u=0. \quad (3.1.39)$$

Now, Eq. (3.1.39) can be rearranged in the factored form which is as follows:

$$\left(\frac{\partial}{\partial t}-\sqrt{\frac{\mathcal{G}_1}{2}}\frac{\partial}{\partial x}\right)\left(\frac{\partial}{\partial t}-\sqrt{\frac{\mathcal{G}_2}{2}}\frac{\partial}{\partial x}\right)\left(\frac{\partial}{\partial t}+\sqrt{\frac{\mathcal{G}_2}{2}}\frac{\partial}{\partial x}\right)\left(\frac{\partial}{\partial t}+\sqrt{\frac{\mathcal{G}_1}{2}}\frac{\partial}{\partial x}\right)u$$
$$+\tau_q\frac{\partial}{\partial t}\left(\frac{\partial}{\partial t}-\sqrt{\frac{\mathcal{H}_1}{2\tau_q}}\frac{\partial}{\partial x}\right)\left(\frac{\partial}{\partial t}-\sqrt{\frac{\mathcal{H}_2}{2\tau_q}}\frac{\partial}{\partial x}\right)\left(\frac{\partial}{\partial t}+\sqrt{\frac{\mathcal{H}_2}{2\tau_q}}\frac{\partial}{\partial x}\right)\left(\frac{\partial}{\partial t}+\sqrt{\frac{\mathcal{H}_1}{2\tau_q}}\frac{\partial}{\partial x}\right)u=0, \tag{3.1.40}$$

where

$$\mathcal{G}_{1,2}=k_2+1+\varepsilon\pm\sqrt{\left(k_2-1+\varepsilon\right)^2+4\varepsilon}$$

and

$$\mathcal{H}_{1,2}=k_1+\tau_q+\varepsilon\tau_q\pm\sqrt{\left(k_1-\tau_q+\varepsilon\tau_q\right)^2+4\varepsilon\tau_q^2}.$$

Hence, let $l=4$, $m=5$, $\varphi=u$ and $\zeta=\tau_q$.

Moreover, it is assumed that

$$v_l=\frac{1}{\sqrt{2}}\begin{cases}\sqrt{\mathcal{G}_1} & \text{if } l=1\\ \sqrt{\mathcal{G}_2} & \text{if } l=2\\ -\sqrt{\mathcal{G}_2} & \text{if } l=3\\ -\sqrt{\mathcal{G}_1} & \text{if } l=4\end{cases} \tag{3.1.41}$$

and

$$r_m=\frac{1}{\sqrt{2\tau_q}}\begin{cases}\sqrt{\mathcal{H}_1} & \text{if } m=1\\ \sqrt{\mathcal{H}_2} & \text{if } m=2\\ 0 & \text{if } m=3\\ -\sqrt{\mathcal{H}_2} & \text{if } m=4\\ -\sqrt{\mathcal{H}_1} & \text{if } m=5.\end{cases} \tag{3.1.42}$$

As described in the previous chapter, the solution under the MGT thermoelasticity theory is exponentially stable if the condition $K > K^*\tau_q$ holds (see Quintanilla (2019)). Further, transforming the relation $K > K^*\tau_q$ to non-dimensional form and dropping the prime for simplicity, the following is found:

$$k_1 > k_2\tau_q. \tag{3.1.43}$$

Now, we observe that $\zeta = \tau_q > 0$, $l = m - 1 = 4$ and from Eqs. (3.1.41) $-$ (3.1.43), it can be easily seen that

$$\sqrt{\frac{\mathcal{H}_1}{2\tau_q}} > \sqrt{\frac{\mathcal{G}_1}{2}} > \sqrt{\frac{\mathcal{H}_2}{2\tau_q}} > \sqrt{\frac{\mathcal{G}_2}{2}} > 0 > -\sqrt{\frac{\mathcal{G}_2}{2}} > -\sqrt{\frac{\mathcal{H}_2}{2\tau_q}} > -\sqrt{\frac{\mathcal{G}_1}{2}} > -\sqrt{\frac{\mathcal{H}_1}{2\tau_q}}. \tag{3.1.44}$$

Thus, by applying Whitham's stability criterion, it is concluded that plane waves propagating in view of the MGT model are stable.

### 3.1.7 Numerical Results and Discussion

In order to have a detailed analysis on the nature of wave components such as phase velocity, specific loss, and penetration depth, numerical computations are performed in this subsection and the asymptotic results of different wave components for both cases of elastic and thermal mode wave are explained by numerical approach. The computation for the values of all these wave components is carried out for intermediate values of frequency $\omega$ under all four cases, namely, Biot classical model, LS model, GN-III model, and MGT model. We determine the numerical values of these wave characteristics by directly solving the Eq. (3.1.14) and with the help of formulas given by Eqs. (3.1.20), (3.1.25), and (3.1.30) using mathematical software (Mathematica). The variations of these wave components with respect to $\omega$ are presented in the different figures. Here,

the copper material is taken and the following values of material constants and physical parameters are considered to achieve numerical results:

$$\lambda = 7.76 \times 10^{10} \text{ kg m}^{-1} \text{ s}^{-2},\ \mu = 3.86 \times 10^{10} \text{ kg m}^{-1} \text{ s}^{-2},\ \rho = 8954 \text{ kg m}^{-3},$$
$$C_E = 383.1 \text{ J kg}^{-1} \text{ K}^{-1},\ \alpha_t = 1.78 \times 10^{-5} \text{ K}^{-1},\ K = 386 \text{ W m}^{-1} \text{ K}^{-1},\ T_0 = 293 \text{ K},$$
$$K^* = 5930.38 \times 10^{10} \text{ W m}^{-1} \text{ K}^{-1} \text{ s}^{-1},\ k_1 = 1,\ k_2 = 1,\ \varepsilon = 0.0168,\ \tau_q = 0.01.$$

To show the figures separately for low frequency and high frequency, we use the part (a) and (b), respectively in each figure. The wave quantities with respect to elastic mode wave and thermal mode wave are represented by the subscripted notations '$E$' and '$T$', respectively. From the figures, it is observed that the limiting behavior of various wave components as derived in previous subsections are perfectly matched with numerical results for MGT model as shown in corresponding figures. This verifies the correctness of our analytical results. We further find the following observations from the analytical and numerical results:

#### 3.1.7.1 Phase velocity

Figs. 3.1.1(a,b) show the phase velocity profiles for elastic mode longitudinal wave in the contexts of all four models, whereas the nature of phase velocity for thermal mode wave is represented by Figs. 3.1.2(a,b). Fig. 3.1.1(a) and Fig. 3.1.1(b) depict the variation of phase velocity for elastic mode wave ($V_E$) in terms of lower values of $\omega$ and higher values of $\omega$, respectively. From Fig. 3.1.1(a), we conclude that in the case of lower range of frequency values, the nature of $V_E$ under the MGT model is similar to the GN-III model, however, it is quite different as compared to the LS and Biot models. From the theoretical result given by Eq. (3.1.23) for lower frequency, it is clear that $V_E$ approaches a finite value (equal to $\frac{1}{\sqrt{W_1}}$) as $\omega \to 0$. The finite value of $V_E$ is approximately 0.9372 under the MGT and GN-III models as $\omega \to 0$. This is

clearly verified from Fig. 3.1.1(a). From Fig. 3.1.1(b), it can be easily noted that phase velocity for elastic mode wave approaches a finite value as $\omega \to \infty$ under all models. In the context of MGT model, $V_E$ starting with a finite value increases slowly with the increase of frequency and tends to its limiting value of 0.99991 after attaining a local maxima at $\omega \approx 205.3$ which also agrees with our analytical results as given by Eq. (3.1.21) reporting that $V_E$ tends to a finite value as $\omega \to \infty$. The limiting value of $V_E$ is same under the MGT and LS models, whereas $V_E$ as predicted by the Biot model and GN-III model approaches a constant value 1. Hence, we conclude that as frequency increases, the profile of $V_E$ under the MGT model differs from the case under the GN-III model and matches very closely with the profile of $V_E$ under the LS model. However, the profiles for the GN-III and Biot's model match together for high-frequency values.

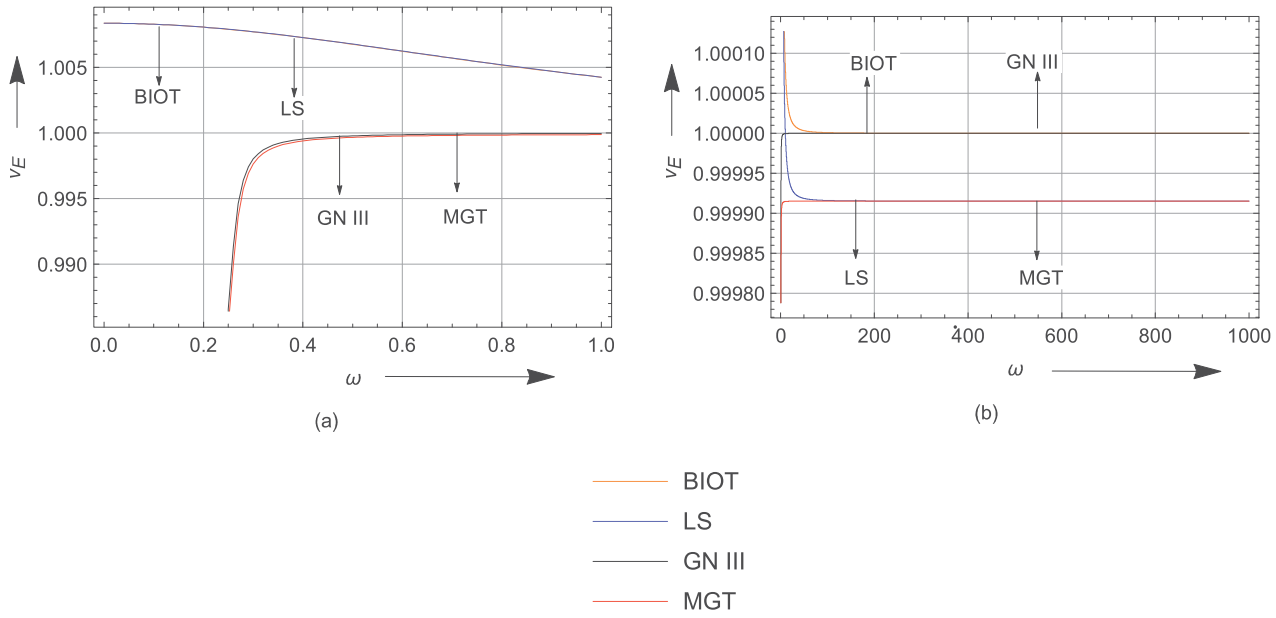


Figure 3.1.1: (a) Variation of phase velocity for elastic mode wave with low frequency. (b) Variation of phase velocity for elastic mode wave with high frequency.

Fig. 3.1.2(a) expresses the variation of phase velocity for thermal mode wave ($V_T$)

with respect to lower values of $\omega$, whereas Fig. 3.1.2(b) expresses the variation of phase velocity for thermal mode wave with respect to higher values of $\omega$. Fig. 3.1.2(a) indicates that for lower range of frequency values, the trend of variation of $V_T$ in the context of MGT model is prominently different from the cases of Biot and LS models. However, in the case of low-frequency values, there is no significant difference in the nature of $V_T$ profiles under the MGT and GN-III models (see Fig. 3.1.2(a)). We further notice that $V_T$ shows a finite value ($V_T \approx 1.0669$) for both cases of MGT and GN-III models as $\omega \to 0$ which agrees with our theoretical results (see Eq. (3.1.24) for the case of MGT model and see Puri (1973), Puri and Jordan (2004) for the cases of LS model and GN-III model). As frequency increases, our analytical results (see Eq. (3.1.22) for the MGT model) as well as numerical results (see Fig. 3.1.2(b)) reveal that $V_T$ under the MGT and LS models reaches a finite value which is approximately 10. In contrast, the thermal mode wave is found to be an increasing function of frequency indicating an infinite speed propagation of thermal mode wave in the cases of Biot and GN-III models (see Fig. 3.1.2(b)). This unrealistic fact of the GN-III model can also be clearly verified with the corresponding result predicted in Puri and Jordan (2004). From numerical observations, we see that under the MGT model, the phase velocity of thermal mode wave increases. Our numerical result for the case of GN-III model matches perfectly with the corresponding result predicted by Puri and Jordan (2004). Further, it is worth mentioning that our numerical result for the LS model is in complete agreement with the result as reported by Puri (1973).

Hence, we conclude that a complete agreement is indicated in the nature of $V_E$ and $V_T$ profiles predicted by the MGT model and GN-III model for the case of lower range of frequency, whereas the nature of $V_E$ and $V_T$ in the MGT and LS models match together as frequency increases. This implies that the effect of parameter $K^*$ is significant for small frequency values and the effect of thermal relaxation parameter is prominent when frequency increases. This is an important observation of the present subchapter.

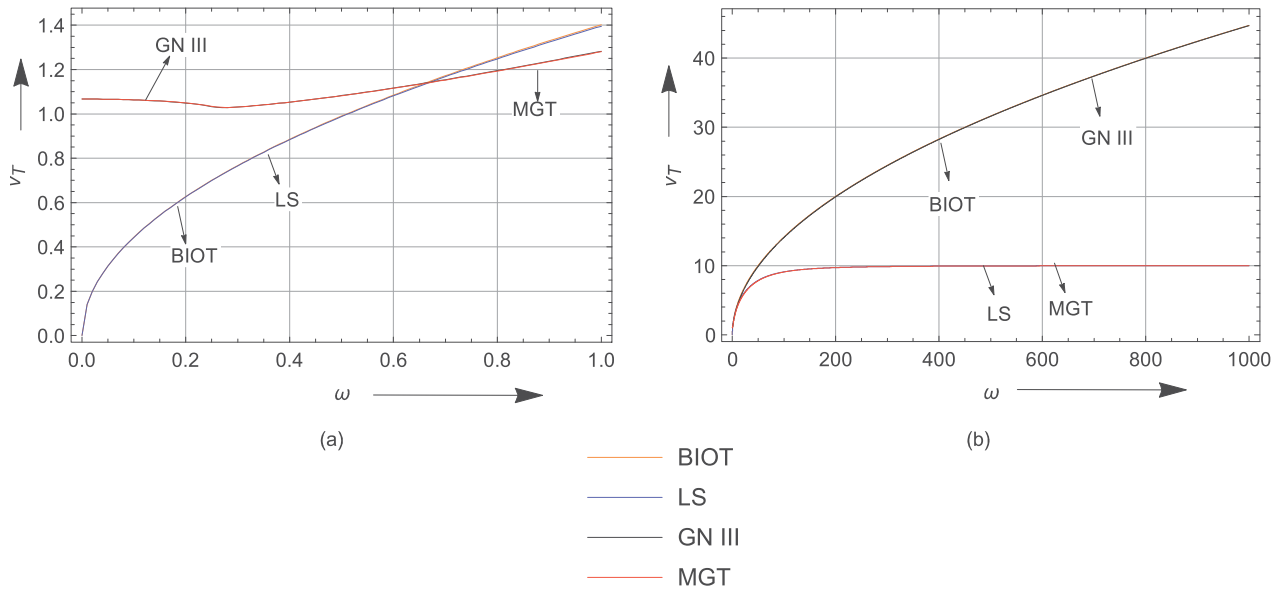


Figure 3.1.2: (a) Variation of phase velocity for thermal mode wave with low frequency. (b) Variation of phase velocity for thermal mode wave with high frequency.

### 3.1.7.2 Specific loss

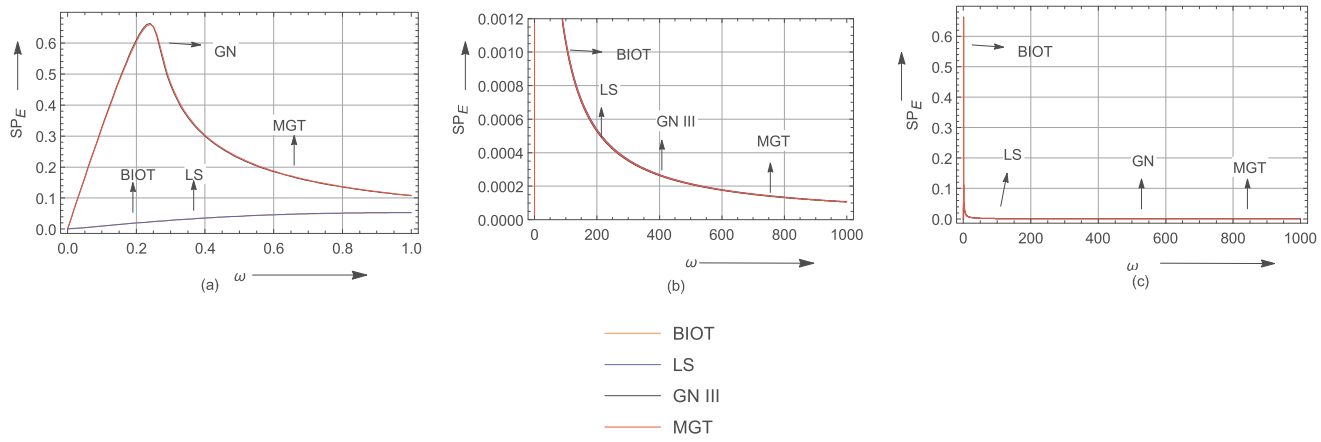


Figure 3.1.3: (a) Variation of specific loss for elastic mode wave with low frequency. (b,c) Variation of specific loss for elastic mode wave with high frequency.

Figs. 3.1.3(a,b,c) and 3.1.4(a,b) describe the variations of specific loss for elastic mode wave and thermal mode wave, respectively in the contexts of the four different models. Fig. 3.1.3(a) indicates that like the phase velocity profile, the specific loss for elastic

mode wave under the MGT and GN-III models behave similarly for lower values of frequency, whereas the nature of specific loss for elastic mode wave predicted by the Biot and LS models is significantly different in comparison to the MGT and GN-III models for the lower range of frequencies. We observe that under all models, $\mathrm{SP}_E \to 0$ as $\omega \to 0$ (see Fig. 3.1.3(a)). This fact is also verified clearly from our analytical results (see Eq. (3.1.28)). Here, Figs. 3.1.3(b,c) present the behavior of specific loss of elastic mode wave for higher frequency, however, Fig. 3.1.3(c) shows the variations when the range of graph is magnified. It is further observed that as frequency increases, the trend of variation of $\mathrm{SP}_E$ under all models (see Figs. 3.1.3(b,c)) matches and show a similar trend to reach zero value. From Figs. 3.1.3(b,c), we conclude that $\mathrm{SP}_E$ tends to 0 as $\omega \to \infty$ in the contexts of all four models. This agrees with our analytical result represented by Eq. (3.1.26) which predicts that $\mathrm{SP}_E$ tends to zero as $\omega \to \infty$. Like the case of GN-III model (see Puri and Jordan (2004)), we observe that $\mathrm{SP}_E$ concerning the MGT model starts with zero and after attaining a local maximum value ($\sim 0.60352$) at $\omega \approx 0.25$, it finally approaches to zero.

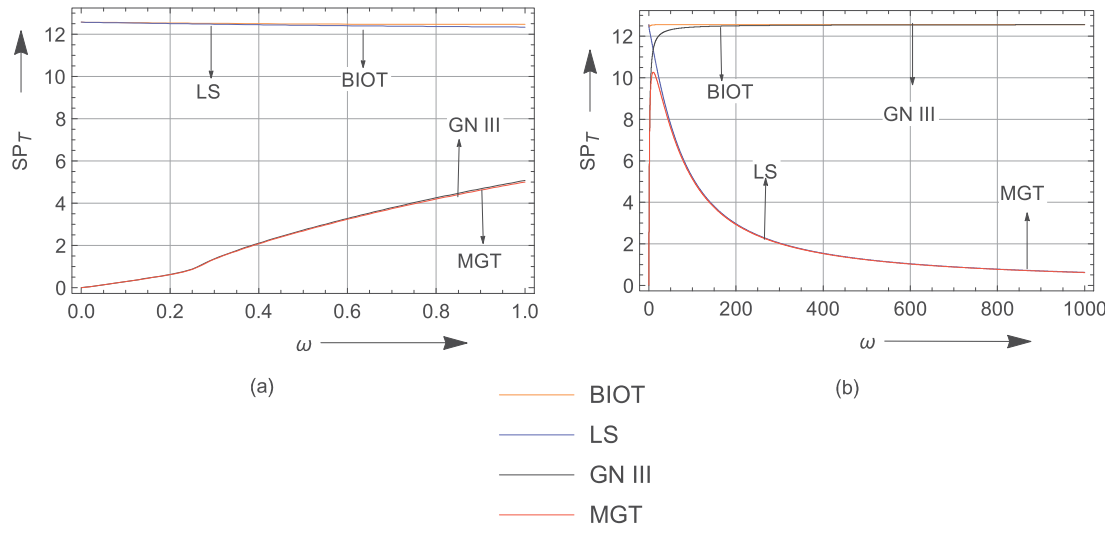


Figure 3.1.4: (a) Variation of specific loss for thermal mode wave with low frequency. (b) Variation of specific loss for thermal mode wave with high frequency.

From Fig. 3.1.4(a), we conclude that specific loss for thermal mode longitudinal wave approaches to 0 as $\omega \to 0$ under the MGT and GN-III models. Thus, we find a perfect match between the numerical results (see Fig. 3.1.4(a)) and analytical results (see Eq. (3.1.29) for the MGT model) indicating that $SP_T$ tends to 0 as $\omega \to 0$. It is observed that in the case of lower values of $\omega$, the trend of variation of $SP_T$ under the MGT model is similar to the GN-III model, however, the MGT model predicts prominently different behavior for this wave field as compared to the Biot and LS models (see Fig. 3.1.4(a)) for the lower range of frequency values. Fig. 3.1.4(b) illustrates that specific loss associated with thermal wave tends to zero as $\omega \to \infty$ in the contexts of MGT and LS models. For the MGT model, this fact is also apparent from the analytical result as described by Eq. (3.1.27). Furthermore, $SP_T$ in view of the MGT model is prominently different from the Biot and GN-III models as $SP_T$ approaches the limiting value of $4\pi$ under the Biot and GN-III models as frequency increases. It is concluded that in the contexts of MGT model, the specific loss associated with thermal wave starts with 0, attains a local maximum value of approximately 10.2638 at $\omega \approx 10.1$ and then again approaches to zero as $\omega \to \infty$. Hence, we observe that the trend of specific loss profiles for both elastic and thermal mode waves in view of the MGT model agrees with the GN-III model and LS model for the lower range of frequency values and higher values of frequency, respectively. Our numerical result for the LS model is found to match with the result as reported by Puri (1973). For the case of GN-III model, our numerical result agrees with the corresponding result predicted by Puri and Jordan (2004).

#### 3.1.7.3 Penetration depth

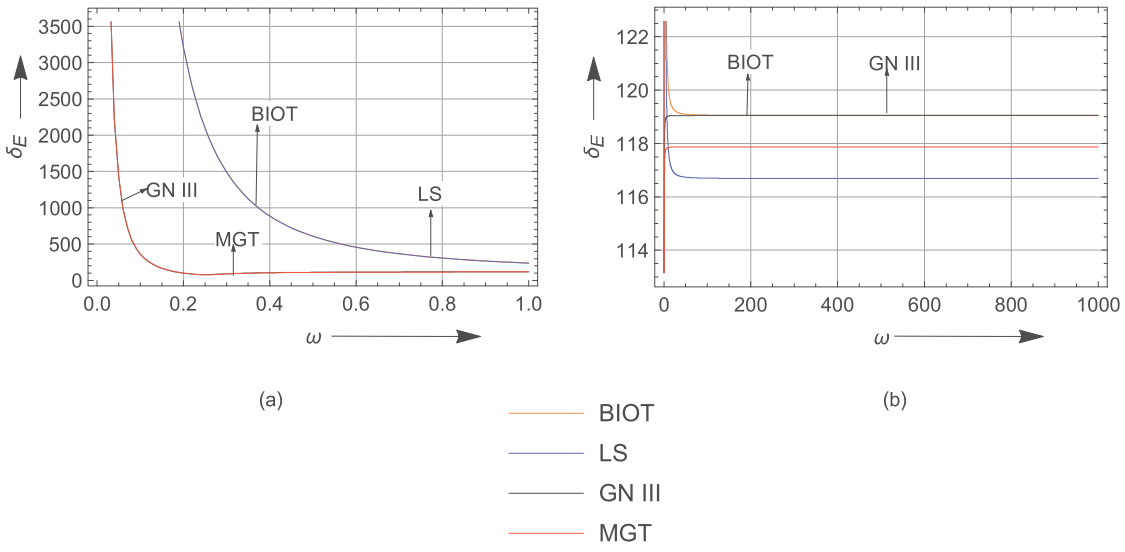


Figure 3.1.5: (a) Variation of penetration depth for elastic mode wave with low frequency. (b) Variation of penetration depth for elastic mode wave with high frequency.

The variations of penetration depth for elastic mode wave and thermal mode wave predicted by four different models are depicted in Figs. 3.1.5(a,b) and 3.1.6(a,b), respectively. Fig. 3.1.5(a) reveals that penetration depth for elastic mode wave follows almost the same nature under the MGT and GN-III models in the case of lower range of frequency values. Numerical results (see Fig. 3.1.5(a)), analytical results given by Eq. (3.1.33) for the MGT model and the results reported for the LS model (see Puri (1973)) and GN-III model (see Puri and Jordan (2004)) indicate that $\delta_E \to \infty$ as $\omega \to 0$ under all four different models. As frequency increases, $\delta_E$ approaches its finite limiting value under all models (see Fig. 3.1.5(b)). This fact is also indicated by our analytical result as given by the Eq. (3.1.31) which reveals that under MGT model, $\delta_E$ approaches its finite limiting value $(\frac{2\sqrt{R_1}}{S_1})$ as $\omega \to \infty$. However, there is a difference in the limiting values of $\delta_E$ as predicted by four different models implying that penetration depth of wave is affected by material parameters. From Fig. 3.1.5(a,b), we observe that $\delta_E$ under the MGT model decreases from infinite value, achieves a local minimum value, approx-

imately 88.7043, at $\omega \approx 0.2$ and then it starts increasing and tends to a finite limiting value of 117.868. This trend of variation in $\delta_E$ is very much similar in the context of GN-III model. Moreover, $\delta_E$ reaches to nearly the same limiting values under these two models. However, this limiting value is significantly different from the limiting value as shown by Biot and GN-III models. Hence, the effect of thermal relaxation parameter on the penetration depth profile for higher frequency values is more prominent.

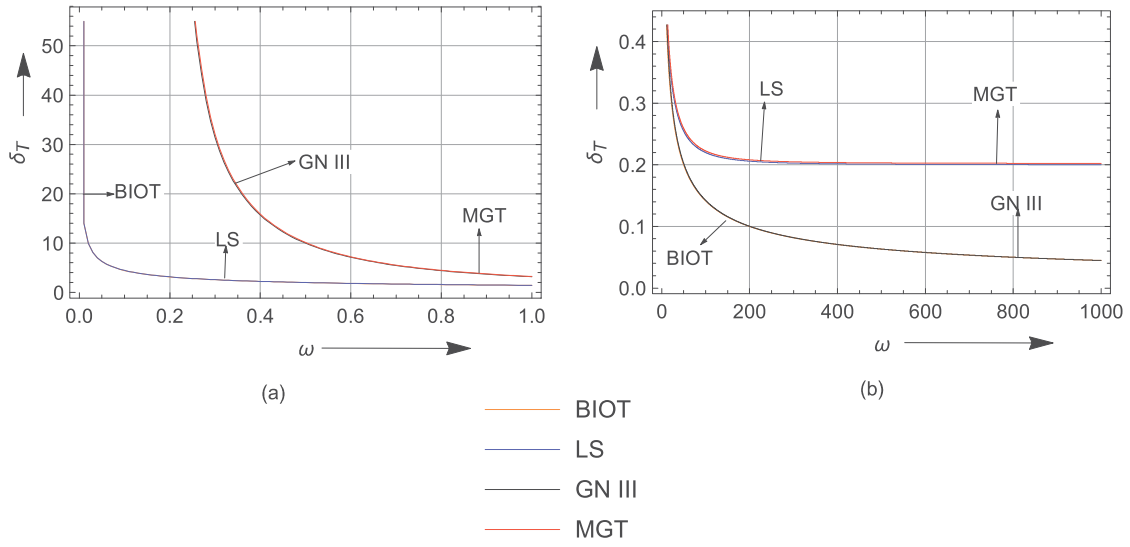


Figure 3.1.6: (a) Variation of penetration depth for thermal mode wave with low frequency. (b) Variation of penetration depth for thermal mode wave with high frequency.

Figs. 3.1.6(a) and 3.1.6(b) demonstrate the variations of penetration depth for thermal mode wave with respect to low frequency and high frequency, respectively. Figs. 3.1.6(a,b) report the similar behavior of $\delta_T$ in the contexts of all four models showing that $\delta_T$ starts with infinite value and thereafter, decreases to its constant limiting value. However, a significant difference is found in the limiting values of penetration depth for thermal mode wave. It can be seen that the limiting value of $\delta_T$ is 0.20207 under the MGT model and LS model, whereas $\delta_T$ approaches to zero as $\omega \to \infty$ in the contexts of Biot model and GN-III model. This fact is also predicted by our analytical result obtained for the MGT model as given by the Eq. (3.1.32) and Eq. (3.1.34). It is to be

observed that $\delta_T$ is a decreasing function of $\omega$ under all four present models (see Figs. 3.1.6(a,b)).

We must emphasize here that our numerical results obtained for the GN-III model are in complete agreement with the result reported by Puri (1973) and our numerical results concerning the case of LS model perfectly match with the corresponding results predicted by Puri and Jordan (2004).

### 3.1.8 Conclusion

In this subchapter, the harmonic plane wave propagation inside a homogeneous and isotropic medium under the Moore-Gibson-Thompson (MGT) thermoelastic model proposed by Quintanilla (2019) is investigated. The transverse wave in this context is found to be unaffected by the thermal field. However, we find the existence of longitudinal wave that is coupled with the thermal and elastic fields. In order to investigate the detailed nature of the longitudinal wave for elastic and thermal modes, the dispersion relation and its solutions are derived. The stability of plane wave propagating through the medium under the new model is analyzed. We further emphasize on the analysis of important wave components such as specific loss, phase velocity, and penetration depth and derive the asymptotic expansions for these wave components in the context of MGT model. Computational work is also carried out to verify and illustrate the theoretical results. The theoretical and numerical results for variations of these wave components are analyzed in detail. With the purpose of investigating the prediction of the MGT model and comparing the results with the corresponding results of other existing models, we study our problem with the unified governing equations of four different models, namely MGT, LS, GN-III, and Biot models. The nature of the wave components under these four models (Biot, LS, GN-III, and MGT) are graphically displayed. The analytical results of the MGT model are found to match perfectly with the numerical results. Various significant facts about the plane wave propagation and

behavior of wave components are highlighted. Some of these facts can be concluded in the following way:

- By applying Whitham's stability criterion, it is found that plane waves propagating in view of the MGT model are stable.

- Phase velocity for elastic mode wave ($V_E$ ) in the contexts of the MGT and GN-III models tends to a finite value of 0.9372 as $\omega \to 0$ which is prominently different as compared to the value predicted by Biot and LS models. As frequency increases, $V_E$ approaches to its approximate finite value of 1 under all four different models. Thus, the trend of variation of $V_E$ for all four models is similar in the case of high-frequency. There is a significant difference in the results of phase velocity of thermal mode wave under different models. This wave field under the MGT model attains local minima at $\omega \approx 0.3$ and approaches its limiting value of 10, that is the same limiting value in the context of LS model. This behavior of $V_T$ is completely different from the cases of Biot and GN-III models as an infinite velocity for thermal mode wave is predicted in these two cases.

- In the same way as in the GN-III model, the specific loss for elastic mode wave under the MGT model starting with zero, reaches a local maximum value of 0.60352 at $\omega \approx 0.25$ and then starts decreasing to approach to zero value. On the other hand, the specific loss for thermal mode wave under the MGT model starts with zero and again tends to zero after attaining a local maximum at $\omega \approx 10.1$ with an approximate value of 10.2638. After attaining extreme value, the specific loss of thermal mode wave decreases and tends to a finite limiting value. This limiting value under the MGT model is the same as the limiting value predicted by the LS model. However, $\mathrm{SP}_T$ for the Biot and GN-III models approaches to $4\pi$ as $\omega \to \infty$.

- Penetration depth for elastic mode wave under the Biot, LS, GN-III, and MGT

models tends to infinity as $\omega$ tends to zero and approaches its finite limiting value under all models as $\omega \to \infty$. Further, the trend of variation of penetration depth for thermal mode wave is almost similar under all models as $\delta_T$ is a decreasing function of $\omega$ in the contexts of four different models and tends to a finite value. However, as frequency increases, the limiting values of $\delta_T$ are observed to be different under MGT and LS models as compared to the other two models (i.e., GN-III and Biot models). As opposed to Biot and GN-III models, $\delta_T$ approaches to 0.20207 as $\omega$ tends to $\infty$ in the contexts of MGT and LS models. This also agrees with the analytical prediction.

- As major findings of the present investigation, it is noted that for the case of lower range of frequency values, the MGT and GN-III models predict similar results for all wave fields like phase velocity, specific loss and penetration depth for both elastic and thermal mode waves. On the other hand, a significant difference is observed in the results of these wave characteristics predicted by the MGT and LS models for lower values of frequency. This implies that the effect of material parameter $K^*$ on wave fields is significant for waves with small range of frequency values. However, in the case of higher range of frequency values, it is investigated that the variation of all these wave characteristics for the elastic mode wave as well as the thermal mode wave under the MGT and LS models are similar in nature, whereas the predictions by the MGT and LS models are significantly different with the predictions by the Biot and GN-III models. Hence, the effect of thermal relaxation parameter on wave components is prominent when frequency increases.

- Like the case of LS model, the MGT model accounts for finite speed of elastic wave as well as thermal mode wave and predicts the realistic nature of wave propagation through the medium. However, the GN-III model does not show finite speed for the thermal mode wave like the case of classical Biot model. This is an important observation of the present study for the MGT model. It is worth

to be mentioned here that the theoretical and numerical results of the MGT model under the present investigation agree with the domain of influence results of MGT model as derived in chapter 2.

## 3.2 Legendre Wavelet Collocation Method for Investigating Thermo-Mechanical Responses on Biological Tissue During Laser Irradiation

### 3.2.1 Introduction[2]

Thermoelasticity is used in a wide range of fields due to its ability to understand and predict material behavior in response to temperature changes. One such application is in the field of biomedical such as treatment response monitoring, cancer treatment, and other medical treatments involving controlled heating of tissues. In cancer treatments, one of the difficulties with thermal treatment is the selective destruction of tumor cells without harming adjacent healthy tissues. To provide high-quality therapeutic care, a grasp of temperature and the distribution of stress in biological tissue is absolutely necessary. Thus, because of the useful application in this field, the present subchapter is motivated to address a problem of biological tissue in the presence of superficial cancer and analyze the thermo-mechanical behavior during laser irradiation. This study is carried out by employing MGT thermoelasticity theory.

To describe the temperature profile in the human forearm, Pennes (1948) was the first to develop a bioheat transfer equation. For the purpose of investigating the thermoelastic response in tumorous tissue for hyperthermia therapy, Ezzat (2020) used a one-dimensional model. Ragab et al. (2021) looked into the thermal reactions in biological spherical tissue for the MGT bioheat conduction model during magnetoma hyperthermia. Some recent investigations that have been performed to reveal the thermo-mechanical responses in generalized bio-thermoelastic models can be found in the articles reported by Jiao and Guo (2009), Li et al. (2020), Wang et al. (2021), Zhang et al. (2021b), and also by Singh and Mukhopadhyay (2023b). In addition to

[2]The content of this chapter is under review in an international journal.

the above mentioned works, pure bioheat transfer models and coupled bio-thermoelastic models are solved utilizing a variety of numerical techniques, including finite difference, finite element and finite element wavelet galerkin methods (see Tung et al. (2009), Gupta et al. (2013), Das et al. (2013), Kumar and Rai (2016), Kumar et al. (2016), Li et al. (2019), Alosaimi et al. (2021)).

Motivated by the above works, the current subchapter seeks to provide a numerical procedure based on the Legendre wavelet method for examining thermo-mechanical interactions in biological tissue caused by laser irradiation. In the case of tumor-normal tissue, coupled equations of the Moore-Gibson-Thompson (MGT) bioheat transfer theory are presented by taking variable material properties into consideration. To solve this generalized model, governing equations involving nonlinear terms are first linearized using the Kirchhoff transformation. Further, the Legendre wavelet approach combined with the method of finite difference is adopted to acquire the numerical solutions for displacement, temperature, and stress. The impacts of varying thermal conductivity and relaxation parameters on the variations of all these field variables and on the tumor-normal tissue interface are discussed and graphically demonstrated. In addition, the discrepancies between the MGT theory and other existing thermoelastic theories (Biot, LS, and GN-III) on transient responses of the present problem are highlighted.

### 3.2.2 Basic Governing Equations

The basic governing equations based on the Moore-Gibson-Thompson (MGT) bioheat transfer model considering temperature-dependent material properties and in absence of any body force, can be taken as follows (Pennes (1948), Quintanilla (2019), Ragab et al. (2021)):

**Equation of motion:**

$$\rho \ddot{u}_i = \sigma_{ij,j}. \tag{3.2.1}$$

**Constitutive relation:**

$$\sigma_{ij} = \lambda e_{kk}\delta_{ij} + 2\mu e_{ij} - \gamma\theta\delta_{ij}. \tag{3.2.2}$$

**Entropy equation:**

$$\rho T_0 S = \rho C_E \theta + T_0 \gamma e_{kk}. \tag{3.2.3}$$

**Energy conservation equation:**

$$q_{i,i} = -\rho T_0 \dot{S} + w_b \rho_b c_b (T_b - T) + q_{\text{met}} + q_{\text{ext}}. \tag{3.2.4}$$

**MGT heat conduction law:**

$$\left(1 + \tau_q \frac{\partial}{\partial t}\right) q = -\left(K(\theta)\nabla\theta + K^*(\theta)\nabla\nu\right). \tag{3.2.5}$$

**Geometrical relation:**

$$e_{ij} = \frac{1}{2}\left(u_{i,j} + u_{j,i}\right). \tag{3.2.6}$$

From Eqs. (3.2.1), (3.2.2) and (3.2.6), the displacement equation of motion can be constructed as follows:

$$\rho \ddot{u}_i = \mu u_{i,jj} + (\lambda + \mu) u_{j,ji} - \gamma \theta_{,i}. \tag{3.2.7}$$

Further, by combining Eqs. (3.2.3)-(3.2.5), the following MGT bioheat transfer equation is obtained:

$$\left(\frac{\partial}{\partial t} + \tau_q \frac{\partial^2}{\partial t^2}\right)\left(\rho C_E \dot{\theta} + T_0 \gamma \dot{e}_{kk} - w_b \rho_b c_b (T_b - T) - q_{\text{met}} - q_{\text{ext}}\right) = \frac{\partial}{\partial t}\left[K(\theta)\nabla\theta + K^*(\theta)\nabla\nu\right]_{,i}, \tag{3.2.8}$$

In above equations, $K(\theta)$ and $K^*(\theta)$ respectively represent the thermal conductivity and the rate of thermal conductivity, which are assumed to be dependent on temperature. $q_{\text{met}}$ denotes the metabolic heat generation in the tissue, $T_b$ denotes the temperature of the blood, $T_b = T_0$ is considered in the current study, $w_b$, $c_b$, $\rho_b$ are the blood perfusion, specific heat of blood, and density of the blood, respectively.

Further, $q_{\text{ext}}$ denotes the external heat source. In the present context, it is taken as a laser heat source presented by Gardner et al. (1996) in the following way:

$$q_{\text{ext}}(x,t) = I_0\mu_a\left[B_1 e^{-\frac{l_1 x}{\delta}} - B_2 e^{-\frac{l_2 x}{\delta}}\right] f(t). \tag{3.2.9}$$

In the preceding equation, $I_0$ denotes the laser intensity, $B_1$, $B_2$, $l_1$, $l_2$ represent the functions of diffuse reflectance $R_d$ which can be found in Gardner et al. (1996) and $\mu_a$ is the coefficient of absorption. It is possible for $f(t)$ to be any type of time-dependent function, including a step function, harmonic function, repeated pulse function, etc. In the present subchapter, $f(t)$ is considered in the following form (Alzahrani and Abbas (2019), Gardner et al. (1996)):

$$f(t) = U(t) - U(t - \tau_p),$$

where $U(t)$ represents the unit step function and $\tau_p$ is the laser exposure time. Also, $\delta$ refers to the laser heat source's penetration depth having the following characteristics (Gardner et al. (1996)):

$$\delta = \frac{1}{\sqrt{3\mu_a(\mu_a + (1-g)\mu_s)}}. \tag{3.2.10}$$

Here, $\mu_s$ denotes the coefficient of scattering and $g$ is the anisotropy factor.

### 3.2.3 Problem Formulation

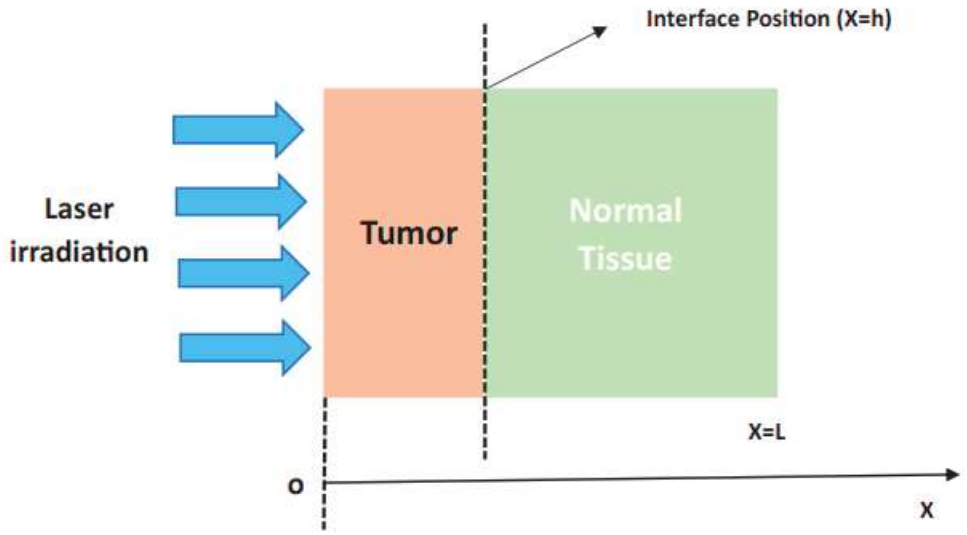


Figure 3.2.1: A tumor-normal tissue model subjected to laser irradiation.

A problem of superficial cancer using laser irradiation is examined in this study. The system of coordinates is set up so that the tumor surface is parallel to the $y$- and $z$-axes, which is assumed to be infinitely long in both axes and it is perpendicular to the $x$-axis. During the time of the treatment, the laser beam utilized in the therapy has a spot size that is significantly greater than the thickness of the biological tissue and it is directly perpendicular to the tumor surface. As shown in Fig. 3.2.1, all functions in the tumor and normal tissues depend simply on the $x$ and time $t$, thus, it is possible to view the problem in one dimension. Also, the tumor-normal tissue interface is considered to be continuous throughout the process. The sub-symbol $i = 1$ denotes the variable in the tumor tissue and $i = 2$ denotes the variable in the normal tissue.

Therefore, the displacements are classified as follows:

$$u_{xi} = u_i(x,t), \;\; u_{yi} = u_{zi} = 0.$$

From Eq. (3.2.6), the following is obtained:

$$e_{xxi} = \frac{\partial u_i}{\partial x}.$$

The equation of motion yields

$$\rho_i \frac{\partial^2 u_i}{\partial t^2} = (\lambda_i + 2\mu_i)\frac{\partial^2 u_i}{\partial x^2} - \gamma_i \frac{\partial \theta_i}{\partial x}. \tag{3.2.11}$$

From Eq. (3.2.8), one can obtain the heat conduction equation as

$$\frac{\partial}{\partial t}\left[K_i(\theta_i)\frac{\partial \theta_i}{\partial x} + K_i^*(\theta_i)\frac{\partial \nu_i}{\partial x}\right]_{,x} = \left(1 + \tau_{qi}\frac{\partial}{\partial t}\right)\left(\rho_i C_{Ei}\frac{\partial^2 \theta_i}{\partial t^2} + T_0\gamma_i \frac{\partial^3 u_i}{\partial t^2 \partial x} + w_{bi}\rho_{bi}c_{bi}\frac{\partial \theta_i}{\partial t}\right.$$
$$\left. - I_0\mu_a g(x)\frac{\partial}{\partial t}\mathscr{F}(x,t)\right), \tag{3.2.12}$$

in which $\mathscr{F}(x,t) = \left(B_1 e^{-\frac{l_1 x}{\delta}} - B_2 e^{-\frac{l_2 x}{\delta}}\right)(U(t) - U(t-\tau_p))$ and in comparison to the high-intensity laser on the tumor surface, metabolic heat generation is ignored.

Next using Eqs. (3.2.2) and (3.2.6), we find the following equation:

$$\sigma_{xxi} = (\lambda_i + 2\mu_i)\frac{\partial u_i}{\partial x} - \gamma_i \theta_i. \tag{3.2.13}$$

#### 3.2.3.1 Boundary and initial conditions

In this subchapter, the Dirichlet temperature boundary condition is adopted, which means the tumor is suddenly heated and its surface ($x = 0$) is stress-free. The rigid boundary of normal tissue is assumed not to be accessible to either heat or elastic waves during the considered time. Thus, the boundary conditions are written as follows (Li

et al. (2020)):

$$\sigma_{xx1}(0,t) = 0, \quad \theta_1(0,t) = \theta_0 \mathscr{H}(t),$$
$$u_2(L,t) = 0, \quad \theta_2(L,t) = 0.$$

where $\theta_0$ is a constant and $\mathscr{H}(t)$ is the Heaviside unit step function.

At the tumor-normal tissue contact, continuous interface conditions are applied.

$$u_1(h,t) = u_2(h,t), \quad \sigma_{xx1}(h,t) = \sigma_{xx2}(h,t),$$
$$\theta_1(h,t) = \theta_2(h,t), \quad q_1(h,t) = q_2(h,t),$$

where $h$ is the interface position.

Furthermore, it is presumable that normal tissue, as well as the tumor tissue, remain initially quiescent. Therefore, initial conditions are given as follows:

$$u_i(x,0) = 0, \quad \frac{\partial u_i}{\partial t}(x,0) = 0, \quad \frac{\partial^2 u_i}{\partial t^2}(x,0) = 0,$$
$$\theta_i(x,0) = 0, \quad \frac{\partial \theta_i}{\partial t}(x,0) = 0, \quad \frac{\partial^2 \theta_i}{\partial t^2}(x,0) = 0.$$

### 3.2.4 Variable Thermal Conductivity

In this subchapter, the parameters $K$ and $K^*$ are considered to be dependent on the temperature as per the following relation (Hetnarski (1986), Abouelregal et al. (2022)):

$$K_i(\theta_i) = K_{i0}(1 + \chi_i \theta_i), \quad K_i^*(\theta_i) = K_{i0}^*(1 + \chi_i \nu_i), \tag{3.2.14}$$

where $\chi_i (i = 1, 2)$ are non-positive small parameters, $K_{i0}$ denote the temperature independent thermal conductivity and $K_{i0}^*$ represents the temperature independent rate of thermal conductivity.

Now, by inserting Eq. (3.2.14) into Eq. (3.2.12), the following nonlinear PDE is

obtained:

$$K_{i0}\frac{\partial}{\partial t}\left[(1+\chi_i\theta_i)\frac{\partial\theta_i}{\partial x}\right]_{,x}+K^*_{i0}\frac{\partial}{\partial t}\left[(1+\chi_i\nu_i)\frac{\partial\nu_i}{\partial x}\right]_{,x}=\left(1+\tau_{qi}\frac{\partial}{\partial t}\right)\left(\rho_i C_{Ei}\frac{\partial^2\theta_i}{\partial t^2}+T_0\gamma_i\frac{\partial^3 u_i}{\partial t^2\partial x}\right.$$
$$\left.+w_{bi}\rho_{bi}c_{bi}\frac{\partial\theta_i}{\partial t}-I_0\mu_a\frac{\partial}{\partial t}\mathscr{F}(x,t)\right). \tag{3.2.15}$$

Because of the nonlinearity of Eq. (3.2.15), it is challenging to solve the coupling Eqs. (3.2.11) and (3.2.15) directly; as a result, the Kirchhoff transformation is introduced as (Hetnarski (1986))

$$\varphi_i=\int_0^{\theta_i}(1+\chi_i\Theta_i)d\Theta_i,\ \ \psi_i=\int_0^{\nu_i}(1+\chi_i\Theta_i)d\Theta_i. \tag{3.2.16}$$

Consequently, we get the following relations:

$$\varphi_i=\theta_i+\frac{1}{2}\chi_i(\theta_i)^2,\quad (\varphi_i)_{,x}=(1+\chi_i\theta_i)\,(\theta_i)_{,x},$$
$$(\varphi_i)_{,xx}=\left\{(1+\chi_i\theta_i)\,(\theta_i)_{,x}\right\}_{,x},\quad \frac{\partial\varphi_i}{\partial t}=(1+\chi_i\theta_i)\frac{\partial\theta_i}{\partial t}, \tag{3.2.17}$$

and

$$\psi_i=\nu_i+\frac{1}{2}\chi_i(\nu_i)^2,\quad (\psi_i)_{,x}=(1+\chi_i\nu_i)\,(\nu_i)_{,x},\quad (\psi_i)_{,xx}=\left\{(1+\chi_i\nu_i)\,(\nu_i)_{,x}\right\}_{,x}. \tag{3.2.18}$$

Substituting Eqs. (3.2.17) and (3.2.18) into Eqs. (3.2.11), (3.2.13) and (3.2.15), it is obtained that

$$\rho_i\frac{\partial^2 u_i}{\partial t^2}=(\lambda_i+2\mu_i)\frac{\partial^2 u_i}{\partial x^2}-\gamma_i\frac{1}{1+\chi_i\theta_i}\frac{\partial\varphi_i}{\partial x}, \tag{3.2.19}$$

$$K_{i0}\frac{\partial}{\partial t}\frac{\partial^2\varphi_i}{\partial x^2}+K^*_{i0}\frac{\partial}{\partial t}\frac{\partial^2\psi_i}{\partial x^2}=\left(1+\tau_{qi}\frac{\partial}{\partial t}\right)\left(\rho_i C_{Ei}\frac{1}{1+\chi_i\theta_i}\frac{\partial^2\varphi_i}{\partial t^2}+T_0\gamma_i\frac{\partial^3 u_i}{\partial t^2\partial x}\right.$$
$$\left.+w_{bi}\rho_{bi}c_{bi}\frac{1}{1+\chi_i\theta_i}\frac{\partial\varphi_i}{\partial t}-I_0\mu_a\frac{\partial}{\partial t}\mathscr{F}(x,t)\right), \tag{3.2.20}$$

$$\sigma_{xxi}=(\lambda_i+2\mu_i)\frac{\partial u_i}{\partial x}-\gamma_i\frac{\sqrt{1+2\chi_i\varphi_i}-1}{\chi_i}. \tag{3.2.21}$$

Using the fact $|\chi_i\theta_i|<<1$ and $|\chi_i\varphi_i|<<1$, $\chi_i\theta_i$ and the higher order term of $\chi_i\varphi_i$ can be neglected for linearity. As a result, Eqs. (3.2.19)-(3.2.21) take the following forms:

$$\rho_i\frac{\partial^2 u_i}{\partial t^2}=(\lambda_i+2\mu_i)\frac{\partial^2 u_i}{\partial x^2}-\gamma_i\frac{\partial\varphi_i}{\partial x}, \tag{3.2.22}$$

$$\left(K_{i0}\frac{\partial}{\partial t}+K^*_{i0}\right)\frac{\partial^2\varphi_i}{\partial x^2}=\left(1+\tau_{qi}\frac{\partial}{\partial t}\right)\left(\rho_i C_{Ei}\frac{\partial^2\varphi_i}{\partial t^2}+T_0\gamma_i\frac{\partial^3 u_i}{\partial t^2\partial x}\right.$$
$$\left.+w_{bi}\rho_{bi}c_{bi}\frac{\partial\varphi_i}{\partial t}-I_0\mu_a\frac{\partial}{\partial t}\mathscr{F}(x,t)\right), \tag{3.2.23}$$

$$\sigma_{xxi}=(\lambda_i+2\mu_i)\frac{\partial u_i}{\partial x}-\gamma_i\varphi_i. \tag{3.2.24}$$

After obtaining $\varphi_i$, the temperature increment can be determined by solving Eq. (3.2.17) as

$$\theta_i=\frac{-1+\sqrt{1+2\chi_i\varphi_i}}{\chi_i}.$$

To simplify the above equations, the non-dimensional parameters and variables are introduced as follows:

$$x^*=\frac{x}{l},\quad (t^*,\tau^*_{qi},\tau^*_p)=\frac{v}{l}(t,\tau_{qi},\tau_p),\quad u^*_i=\frac{\lambda_1+2\mu_1}{l\gamma_1(T_\infty-T_0)}u_i,\quad (\theta^*_i,\varphi^*_i)=\frac{1}{T_\infty-T_0}(\theta_i,\varphi_i),$$
$$\sigma^*_{xxi}=\frac{\sigma_{xxi}}{\gamma_1(T_\infty-T_0)},\quad q^*_i=\frac{q_i}{K_{10}(T_\infty-T_0)},\quad (l^*_1,l^*_2)=\frac{l}{\delta}(l_1,l_2),\quad v=\sqrt{\frac{(\lambda_1+2\mu_1)}{\rho_1}},$$

where $v$ and $l$ denote the velocity and characteristic length, respectively. $T_\infty$ denotes the temperature of thermal therapy applied on the tumor surface. For the sake of brevity, the asterisk symbol has been dropped in the following equations. Therefore,

Eqs. (3.2.22)-(3.2.24) can be represented in the non-dimensional forms as

$$\frac{\partial^2 u_i}{\partial t^2} = a_{1i}\frac{\partial^2 u_i}{\partial x^2} - a_{2i}\frac{\partial \varphi_i}{\partial x}, \tag{3.2.25}$$

$$\left(\frac{\partial}{\partial t} + a_{3i}\right)\frac{\partial^2 \varphi_i}{\partial x^2} = \left(1 + \tau_{qi}\frac{\partial}{\partial t}\right)\left(a_{4i}\frac{\partial^2 \varphi_i}{\partial t^2} + a_{5i}\frac{\partial^3 u_i}{\partial t^2 \partial x} + a_{6i}\frac{\partial \varphi_i}{\partial t} - a_{7i}\frac{\partial}{\partial t}\mathscr{F}(x,t)\right), \tag{3.2.26}$$

$$\sigma_{xxi} = a_{8i}\frac{\partial u_i}{\partial x} - a_{9i}\varphi_i, \tag{3.2.27}$$

where

$$a_{1i} = \frac{(\lambda_i + 2\mu_i)}{\rho_i v^2}, \quad a_{2i} = \frac{\gamma_i(\lambda_1 + 2\mu_1)}{\rho_i v^2 \gamma_1}, \quad a_{3i} = \frac{K^*_{i0} l}{K_{i0} v}, \quad a_{4i} = \frac{\rho_i C_{Ei} l v}{K_{i0}}, \quad a_{5i} = \frac{T_0 \gamma_i l v \gamma_1}{K_{i0}(\lambda_1 + 2\mu_1)},$$
$$a_{6i} = \frac{w_{bi}\rho_{bi}c_{bi}l^2}{K_{i0}}, \quad a_{7i} = \frac{I_0 \mu_a l^2}{K_{i0}(T_\infty - T_0)}, \quad a_{8i} = \frac{(\lambda_i + 2\mu_i)}{\lambda_1 + 2\mu_1}, \quad a_{9i} = \frac{\gamma_i}{\gamma_1}.$$

The corresponding dimensionless boundary conditions take the following forms:

$$\begin{aligned} &\sigma_{xx1}(0,t) = 0, \quad \varphi_1(0,t) = \varphi_0 \mathscr{H}(t), \\ &u_2(L,t) = 0, \quad \varphi_2(L,t) = 0, \end{aligned} \tag{3.2.28}$$

where $\varphi_0 = \theta_0 + \frac{\chi_1}{2}\theta_0^2$ and interfacial conditions can be rewritten as

$$\begin{aligned} &u_1(h,t) = u_2(h,t), \quad \sigma_{xx1}(h,t) = \sigma_{xx2}(h,t), \\ &\varphi_1(h,t) = \varphi_2(h,t), \quad q_1(h,t) = q_2(h,t), \end{aligned} \tag{3.2.29}$$

Also, the initial conditions can be expressed as

$$\begin{aligned} &u_i(x,0) = 0, \quad \frac{\partial u_i}{\partial t}(x,0) = 0, \quad \frac{\partial^2 u_i}{\partial t^2}(x,0) = 0, \\ &\varphi_i(x,0) = 0, \quad \frac{\partial \varphi_i}{\partial t}(x,0) = 0, \quad \frac{\partial^2 \varphi_i}{\partial t^2}(x,0) = 0. \end{aligned} \tag{3.2.30}$$

### 3.2.5 Legendre Wavelets

Wavelets are a family of functions that are made up of translation and dilation of a single function known as the mother wavelet $\Psi(x)$. The family of continuous wavelets results from continuously varying dilation parameter $a$ and translation parameter $b$ as follows (Daubechies (1992))

$$\Psi_{a,b}(x) = |a|^{-1/2}\Psi\left(\frac{x-b}{a}\right),$$

where $a, b \in \mathbb{R}$ and $a \neq 0$. Legendre wavelets $\Psi_{m,n}(x)$ defined on the interval $[0, 1)$ are given as follows (Liu and Lin (2009)):

$$\Psi_{m,n}(x) = \begin{cases} \sqrt{\frac{2n+1}{2}}2^{\frac{k}{2}}L_n(2^k x - \hat{m}), & \frac{\hat{m}-1}{2^k} \leq x < \frac{\hat{m}}{2^k} \\ 0, & \text{otherwise} \end{cases}, \tag{3.2.31}$$

Therefore, four arguments are present in Legendre wavelets $\Psi(n, k, \hat{m}, x)$, where $x$ is normalized time, $k \in \mathbb{N}$, $m = 1, 2, ..., 2^{k-1}$, $\hat{m} = 2m-1$ and $n = 0, 1, 2, ..., N-1$ denotes the order of Legendre polynomial $L_n(x)$. Here, the coefficient $\sqrt{\frac{2n+1}{2}}$ is considered for orthonormality.

#### 3.2.5.1 Function approximation

A square integrable function $f(x)$ defined on the interval $[0, 1)$ can be expressed in terms of Legendre wavelets as (Liu and Lin (2009))

$$f(x) = \sum_{m=1}^{\infty}\sum_{n=0}^{\infty} \alpha_{m,n}\Psi_{m,n}(x), \tag{3.2.32}$$

where $\alpha_{m,n}$ are wavelet coefficients that can be calculated using the inner product $\langle f(x), \Psi_{m,n}(x)\rangle$. If the infinite series represented by Eq. (3.2.32) is truncated, it takes

the following form:

$$f(x) \cong \sum_{m=1}^{2^{k-1}} \sum_{n=0}^{N-1} \alpha_{m,n} \Psi_{m,n}(x). \tag{3.2.33}$$

We use the following for a more compact notation:

$$f(x) \cong \sum_{r=1}^{\hat{n}} \alpha_r \Psi_r(x) = A^T \Psi(x), \tag{3.2.34}$$

where $A$ and $\Psi(x)$ are $\hat{n} = 2^{k-1}N$ column vectors specified as

$$A = \left[\alpha_{1,0}, \alpha_{1,1}, ..., \alpha_{1,N-1}, \alpha_{2,0}, ..., \alpha_{2,N-1}, ..., \alpha_{2^{k-1},0}, \alpha_{2^{k-1},1}, ..., \alpha_{2^{k-1},N-1}\right]^T,$$
$$\Psi(x) = \left[\Psi_{1,0}, \Psi_{1,1}, ..., \Psi_{1,N-1}, \Psi_{2,0}, ..., \Psi_{2,N-1}, ..., \Psi_{2^{k-1},0}, \Psi_{2^{k-1},1}, ..., \Psi_{2^{k-1},N-1}\right]^T.$$

#### 3.2.5.2 Convergence of Legendre wavelets

**Theorem** (Liu and Lin (2009)) If the second-order derivative of a continuous function $f(x)$ defined on $[0, 1)$ is bounded, then it can be expressed as an infinite sum of Legendre wavelets and the expansion of $f(x)$ converges uniformly to it, i.e.

$$f(x) = \sum_{m=1}^{\infty} \sum_{n=0}^{\infty} \alpha_{m,n} \Psi_{m,n}(x).$$

**Proof** (see Liu and Lin (2009))

### 3.2.6 Solution Method

For the solution of the present problem as stated in subsection 3.2.3, the finite-difference approach and Legendre wavelet method are employed to discretize the time domain and the space domain, respectively.

#### 3.2.6.1 Time discretization

To discretize the time domain, we divide the interval $[0, T]$ into $M$ subintervals of equal length and define the following as in Oruç et al. (2015):

$$t_j = j\Delta t, \quad 0 \leq j \leq M, \ j \in \mathbb{Z},$$

where $T$ denotes the final time for $t$ and $\Delta t = \frac{T}{M}$ is the step size for $t$.

To solve further, the following new variables are introduced:

$$\frac{\partial u}{\partial t} = w_i, \quad \frac{\partial}{\partial t}\left(\frac{\partial u_i}{\partial x}\right) = v_i, \quad \frac{\partial v_i}{\partial t} = b_i, \quad \frac{\partial \varphi_i}{\partial t} = d_i, \quad \frac{\partial d_i}{\partial t} = z_i. \tag{3.2.35}$$

Using Eqs. (3.2.35), (3.2.25) and (3.2.26) can be rewritten in the following way:

$$\frac{\partial w_i}{\partial t} = a_{1i}\frac{\partial^2 u_i}{\partial x^2} - a_{2i}\frac{\partial \varphi_i}{\partial x}, \tag{3.2.36}$$

$$\left(\frac{\partial}{\partial t} + a_{3i}\right)\frac{\partial^2 \varphi_i}{\partial x^2} = \left(1 + \tau_{qi}\frac{\partial}{\partial t}\right)\left(a_{4i}z_i + a_{5i}b_i + a_{6i}d_i - a_{7i}R(x,t)\right), \tag{3.2.37}$$

where $R(x,t) = \frac{\partial}{\partial t}\mathscr{F}(x,t)$. Now, making use of the finite difference to approximate time derivatives and averaging the other terms in the aforementioned Eqs. (3.2.35)-(3.2.37), we arrive at

$$\begin{aligned}
\frac{(u_i)_{j+1} - (u_i)_j}{\Delta t} &= \frac{(w_i)_{j+1} + (w_i)_j}{2}, \\
\frac{((u_i)_x)_{j+1} - ((u_i)_x)_j}{\Delta t} &= \frac{(v_i)_{j+1} + (v_i)_j}{2}, \\
\frac{(v_i)_{j+1} - (v_i)_j}{\Delta t} &= \frac{(b_i)_{j+1} + (b_i)_j}{2}, \\
\frac{(\varphi_i)_{j+1} - (\varphi_i)_j}{\Delta t} &= \frac{(d_i)_{j+1} + (d_i)_j}{2}, \\
\frac{(d_i)_{j+1} - (d_i)_j}{\Delta t} &= \frac{(z_i)_{j+1} + (z_i)_j}{2},
\end{aligned}$$

$$\frac{(w_i)_{j+1}-(w_i)_j}{\Delta t}=a_{1i}\frac{((u_i)_{xx})_{j+1}+((u_i)_{xx})_j}{2}-a_{2i}\frac{((\varphi_i)_x)_{j+1}+((\varphi_i)_x)_j}{2},$$
$$\frac{((\varphi_i)_{xx})_{j+1}-((\varphi_i)_{xx})_j}{\Delta t}+a_{3i}\left\{\frac{((\varphi_i)_{xx})_{j+1}+((\varphi_i)_{xx})_j}{2}\right\}=a_{4i}\frac{(z_i)_{j+1}+(z_i)_j}{2}+a_{4i}\tau_{qi}\frac{(z_i)_{j+1}-(z_i)_j}{\Delta t}$$
$$+a_{5i}\frac{(b_i)_{j+1}+(b_i)_j}{2}+a_{5i}\tau_{qi}\frac{(b_i)_{j+1}-(b_i)_j}{\Delta t}+a_{6i}\frac{(d_i)_{j+1}+(d_i)_j}{2}$$
$$+a_{6i}\tau_{qi}\frac{(d_i)_{j+1}-(d_i)_j}{\Delta t}-a_{7i}R_{j+1/2}-a_{7i}\tau_{qi}R_{j-1/2}.$$

Simplifying the aforementioned equations leads us to

$$2(u_i)_{j+1}-\Delta t(w_i)_{j+1}=2(u_i)_j+\Delta t(w_i)_j, \tag{3.2.38}$$
$$2\left((u_i)_x\right)_{j+1}-\Delta t(v_i)_{j+1}=2\left((u_i)_x\right)_j+\Delta t(v_i)_j, \tag{3.2.39}$$
$$2(v_i)_{j+1}-\Delta t(b_i)_{j+1}=2(v_i)_j+\Delta t(b_i)_j, \tag{3.2.40}$$
$$2(\varphi_i)_{j+1}-\Delta t(d_i)_{j+1}=2(\varphi_i)_j+\Delta t(d_i)_j, \tag{3.2.41}$$
$$2(d_i)_{j+1}-\Delta t(z_i)_{j+1}=2(d_i)_j+\Delta t(z_i)_j, \tag{3.2.42}$$
$$2(w_i)_{j+1}-a_{1i}\Delta t\left((u_i)_{xx}\right)_{j+1}+a_{2i}\Delta t\left((\varphi_i)_x\right)_{j+1}=2(w_i)_j+a_{1i}\Delta t\left((u_i)_{xx}\right)_j-a_{2i}\Delta t\left((\varphi_i)_x\right)_j, \tag{3.2.43}$$
$$A_1\left((\varphi_i)_{xx}\right)_{j+1}-a_{4i}A_2(z_i)_{j+1}-a_{5i}A_2(b_i)_{j+1}-a_{6i}A_2(d_i)_{j+1}=A_3\left((\varphi_i)_{xx}\right)_j+a_{4i}A_4(z_i)_j$$
$$+a_{5i}A_4(b_i)_j+a_{6i}A_4(d_i)_j-2\Delta t a_{7i}\left(R_{j+1/2}+\tau_{qi}R_{j-1/2}\right), \tag{3.2.44}$$

where the following notations are used:

$(u_i)_{j+1}=u_i(x,t_{j+1})$, $A_1=(2+a_{3i}\Delta t)$, $A_2=(\Delta t+2\tau_{qi})$, $A_3=(2-a_{3i}\Delta t)$, $A_4=(\Delta t-2\tau_{qi})$, $R_{j+1/2}=\frac{R(x,t_{j+1})+R(x,t_j)}{2}$ and $R_{j-1/2}=\frac{R(x,t_{j+1})-R(x,t_j)}{\Delta t}$.

Making use of the same time discretization scheme, corresponding boundary and interface conditions take the following forms:

$$\sigma_{xx1}(0,t_{j+1})=0,\quad \varphi_1(0,t_{j+1})=\varphi_0\mathscr{H}(t_{j+1}), \tag{3.2.45}$$

$$u_2(L,t_{j+1})=0,\quad \varphi_2(L,t_{j+1})=0, \tag{3.2.46}$$

$$u_1(h,t_{j+1})=u_2(h,t_{j+1}),\quad \sigma_{xx1}(h,t_{j+1})=\sigma_{xx2}(h,t_{j+1}), \tag{3.2.47}$$

$$\varphi_1(h,t_{j+1})=\varphi_2(h,t_{j+1}),\quad q_1(h,t_{j+1})=q_2(h,t_{j+1}). \tag{3.2.48}$$

#### 3.2.6.2 Space discretization by Legendre wavelets

In order to use the wavelet approach, the highest order derivative of unknown functions which appears in the above equations is approximated by Legendre wavelet. Next, the unknown function itself as well as its lower-order derivatives can be retrieved through the use of boundary conditions and sequential integration. Consequently, we start by introducing the following notations (Oruç et al. (2015)):

$$p_{r,1}(x)=\int_0^x \Psi_r(\zeta)d\zeta, \tag{3.2.49}$$

$$p_{r,2}(x)=\int_0^x p_{r,1}(\zeta)d\zeta. \tag{3.2.50}$$

According to the Legendre wavelet method, highest order derivatives $((u_i)_{xx})_{j+1}$ and $((\varphi_i)_{xx})_{j+1}$ $(i=1,2)$ can be expanded as

$$\left(\frac{\partial^2 u_i}{\partial x^2}\right)_{j+1}(x)=\sum_{r=1}^{\hat{n}} g_r^i\Psi_r(x), \tag{3.2.51}$$

$$\left(\frac{\partial^2 \varphi_i}{\partial x^2}\right)_{j+1}(x)=\sum_{r=1}^{\hat{n}} h_r^i\Psi_r(x), \tag{3.2.52}$$

where $g_r^i$ and $h_r^i$ are the wavelet coefficients. Integrating Eq. (3.2.51) with respect to $x$ from 0 to $x$ and considering Eq. (3.2.49), it is found that

$$\left(\frac{\partial u_i}{\partial x}\right)_{j+1}(x)=\sum_{r=1}^{\hat{n}} g_r^i p_{r,1}(x)+\left(\frac{\partial u_i}{\partial x}\right)_{j+1}(0)\,. \tag{3.2.53}$$

Now, if Eq. (3.2.53) is integrated once again from 0 to $x$ with respect to $x$, we acquire the equation shown below:

$$(u_i)_{j+1}(x) = \sum_{r=1}^{\hat{n}} g_r^i p_{r,2}(x) + x\left(\frac{\partial u_i}{\partial x}\right)_{j+1}(0) + (u_i)_{j+1}(0). \tag{3.2.54}$$

Similarly, Eq. (3.2.52) yields the following:

$$\left(\frac{\partial \varphi_i}{\partial x}\right)_{j+1}(x) = \sum_{r=1}^{\hat{n}} h_r^i p_{r,1}(x) + \left(\frac{\partial \varphi_i}{\partial x}\right)_{j+1}(0). \tag{3.2.55}$$

$$(\varphi_i)_{j+1}(x) = \sum_{r=1}^{\hat{n}} h_r^i p_{r,2}(x) + x\left(\frac{\partial \varphi_i}{\partial x}\right)_{j+1}(0) + (\varphi_i)_{j+1}(0). \tag{3.2.56}$$

The Legendre wavelet is now used to approximate the other functions $v_i$, $w_i$, $b_i$, $d_i$ and $z_i$ in the following way:

$$(v_i)_{j+1}(x) = \sum_{r=1}^{\hat{n}} V_r^i \Psi_r(x), \tag{3.2.57}$$

$$(w_i)_{j+1}(x) = \sum_{r=1}^{\hat{n}} W_r^i \Psi_r(x), \tag{3.2.58}$$

$$(b_i)_{j+1}(x) = \sum_{r=1}^{\hat{n}} B_r^i \Psi_r(x), \tag{3.2.59}$$

$$(d_i)_{j+1}(x) = \sum_{r=1}^{\hat{n}} D_r^i \Psi_r(x), \tag{3.2.60}$$

$$(z_i)_{j+1}(x) = \sum_{r=1}^{\hat{n}} Z_r^i \Psi_r(x). \tag{3.2.61}$$

In the above equations, $\left(\frac{\partial u_i}{\partial x}\right)_{j+1}(0)$, $(u_i)_{j+1}(0)$, $\left(\frac{\partial \varphi_i}{\partial x}\right)_{j+1}(0)$ and $(\varphi_i)_{j+1}(0)$ $(i = 1, 2)$ are all unknowns that can be determined with the use of boundary and interface conditions. Substituting Eqs. (3.2.53)-(3.2.56) into the boundary conditions and interface

conditions Eqs. (3.2.45)-(3.2.48), we arrive at

$$\left(\frac{\partial u_1}{\partial x}\right)_{j+1}(0) = \frac{a_{91}}{a_{81}}\varphi_0 \mathscr{H}(t_{j+1}), \tag{3.2.62}$$

$$\sum_{r=1}^{\hat{n}} g_r^2 p_{r,2}(L) + L\left(\frac{\partial u_2}{\partial x}\right)_{j+1}(0) + (u_2)_{j+1}(0) = 0, \tag{3.2.63}$$

$$\sum_{r=1}^{\hat{n}} h_r^2 p_{r,2}(L) + L\left(\frac{\partial \varphi_2}{\partial x}\right)_{j+1}(0) + (\varphi_2)_{j+1}(0) = 0, \tag{3.2.64}$$

$$\sum_{i=1}^{2}(-1)^{i-1}\left[\sum_{r=1}^{\hat{n}} g_r^i p_{r,2}(h) + h\left(\frac{\partial u_i}{\partial x}\right)_{j+1}(0) + (u_i)_{j+1}(0)\right] = 0, \tag{3.2.65}$$

$$\sum_{i=1}^{2}(-1)^{i-1}\left[a_{8i}\left(\frac{\partial u_i}{\partial x}\right)_{j+1}(h) - a_{9i}(\varphi_i)_{j+1}(h)\right] = 0, \tag{3.2.66}$$

$$\sum_{i=1}^{2}(-1)^{i-1}\left[\sum_{r=1}^{\hat{n}} h_r^i p_{r,2}(h) + h\left(\frac{\partial \varphi_i}{\partial x}\right)_{j+1}(0) + (\varphi_i)_{j+1}(0)\right] = 0, \tag{3.2.67}$$

$$\sum_{i=1}^{2}(-1)^{i-1}\left(\frac{\Delta t K_{i0}^* + 2K_{i0}}{\Delta t + 2\tau_{qi}}\right)\left(\frac{\partial \varphi_i}{\partial x}\right)_{j+1}(h) = 0. \tag{3.2.68}$$

By solving Eqs. (3.2.62)-(3.2.68), the desired unknowns $\left(\frac{\partial u_i}{\partial x}\right)_{j+1}(0)$, $(u_i)_{j+1}(0)$, $\left(\frac{\partial \varphi_i}{\partial x}\right)_{j+1}(0)$ and $(\varphi_i)_{j+1}(0)$ for tumor and normal tissues can be calculated. Finally, by plugging Eqs. (3.2.51)-(3.2.61) into Eqs. (3.2.38)-(3.2.44) and discretizing the space variable $x$ with the use of collocation points $\frac{2r-1}{2\hat{n}}$, $r = 1, 2, ..., \hat{n}$, a system of algebraic equations is acquired. The matrix representation of that linear system can be defined as follows:

$$P\boldsymbol{X} = \boldsymbol{\Lambda},$$

where $P$ and $\boldsymbol{\Lambda}$ are known matrices of order $2\hat{n} \times 2\hat{n}$ and $2\hat{n} \times 1$, respectively. $\boldsymbol{X}$ is a matrix of order $2\hat{n} \times 1$ and its elements are wavelet coefficients. Afterward, by successively putting these wavelet coefficients into the corresponding Eqs. (3.2.51)-(3.2.61), the new values of $(u_i)_{xx}$, $(u_i)_x$, $u_i$, $(\varphi_i)_{xx}$, $(\varphi_i)_x$, $\varphi_i$, $v_i$, $w_i$, $b_i$, $d_i$ and $z_i$ $(i = 1, 2)$ can be constructed at each time level. Initial conditions are used to begin this computation. This iteration procedure is continued in this way until the required time

level is reached. This completes the solution to the present problem.

### 3.2.7 Numerical Results

In this subsection, numerical results for the present problem are determined by implementing the Legendre wavelet-collocation approach as discussed above. To carry out numerical computation and display the results, MATLAB software is used. We discuss the effects of the variable thermal conductivity and the thermal relaxation parameters on thermoelastic responses of biological tissue and compare the prediction of various generalized thermoelasticity theories (MGT, Biot, LS, and GN-III) for thermal and elastic reactions with the help of various graphical plots for the distributions of physical fields. The dimensionless length of the model is $L = 1$, while the dimensionless thickness $h$ of tumor tissue is considered to be 0.2. For numerical computation, thermophysical properties of blood, tumor tissue, and normal tissue are mentioned in Table 3.1 (Ragab et al. (2021), Li et al. (2020)) and the parameters of the laser heat source are given in Table 3.2 (Alzahrani and Abbas (2019)). We demonstrate the results for the values of $k = 1$, $N = 6$ and time step size $\Delta t = 0.01$.

| | | | |
|---|---|---|---|
| Blood | $c_b = 3770\,\mathrm{J/kgK}$ | $\rho_b = 1060\,\mathrm{kg/m^3}$ | $T_0 = T_b = 310\mathrm{K}$ |
| Tumor | $C_{E1} = 2540\,\mathrm{J/kgK}$ | $\rho_1 = 1660\,\mathrm{kg/m^3}$ | $w_{b1} = 0.009/\mathrm{s}$ |
| | $\alpha_{t1} = 1 \times 10^{-4}/\mathrm{K}$ | $K_{10} = 0.778\,\mathrm{W/mK}$ | $K^*_{10} = 17\,\mathrm{W/smK}$ |
| | $\lambda_1 = 2.481 \times 10^7\,\mathrm{kg/ms^2}$ | $\mu_1 = 1.034 \times 10^6\,\mathrm{kg/ms^2}$ | |
| Normal tissue | $C_{E2} = 2540\,\mathrm{J/kgK}$ | $\rho_2 = 1000\,\mathrm{kg/m^3}$ | $w_{b2} = 0.00018/\mathrm{s}$ |
| | $\alpha_{t2} = 1 \times 10^{-4}/\mathrm{K}$ | $K_{20} = 0.642\,\mathrm{W/mK}$ | $K^*_{20} = 16\,\mathrm{W/mK}$ |
| | $\lambda_2 = 8.27 \times 10^7\,\mathrm{kg/ms^2}$ | $\mu_2 = 3.446 \times 10^6\,\mathrm{kg/ms^2}$ | |

Table 3.1: Material constants of biological tissue.

| Parameters | Value |
|---|---|
| Anisotropy factor ($g$) | 0.9 |
| Scattering coefficient ($\mu_s$) | $12000\,\mathrm{m}^{-1}$ |
| Absorption coefficient ($\mu_a$) | $40\,\mathrm{m}^{-1}$ |
| Laser intensity ($I_0$) | $3 \times 10^5\,\mathrm{Wm}^{-2}$ |
| Diffuse reflectance ($R_d$) | 0.05 |
| $B_1$ | $3.09 + 5.44R_d - 2.12e^{-21.5R_d}$ |
| $B_2$ | $2.09 - 1.47R_d - 2.12e^{-21.5R_d}$ |
| $l_1$ | $1 - \left(1 - \frac{1}{\sqrt{3}}\right) e^{-20.1R_d}$ |
| $l_2$ | $1.63e^{3.4R_d}$ |

Table 3.2: Parameters of the laser heat source.

Figs. 3.2.3-3.2.14 illustrate the behavior of displacement, temperature, and stress with the distance $x$. These figures reveal that the most affected region for all field variables is upto the tumor-normal tissue interface position and they are identically zero after the interface position. Consequently, these figures demonstrate that all the field variables meet the boundary conditions and the proposed numerical scheme is successfully implemented. The displacement field is found to show a negative numerical value inside the tumor region and thereafter it tends to zero value. The temperature is shown to start at its maximum value at $x = 0$ and gradually decline to zero as we approach the end of the boundary. However, in the affected region, temperature shows a local minimum and a local maximum value. As displayed by the figures, stress begins at 0, climbs until it reaches its peak, and then starts decreasing to tend to zero as we move closer to $x = 1$.

#### 3.2.7.1 Convergence and validation of the present numerical scheme

For the proposed method based on the Legendre wavelet, pointwise convergence studies have been carried out to show the efficiency. The tabular outcomes of pointwise convergence for the present approach are shown in Table 3.3. For numerical computation, the proposed approach is tested for various values of $N$ with $k = 1$, time step size $\Delta t = 0.01$

and values of other parameters are preserved as specified above. From Table 1, one can clearly observe that $N = 6$ is enough to achieve convergence.

| $N$ | Displacement ($u$) | Temperature ($\theta$) | Stress ($\sigma$) |
|---|---|---|---|
| 1 | −0.0065 | 0.0346 | 0.0106 |
| 2 | −0.0028 | 0.0280 | 0.0192 |
| 3 | −0.0010 | 0.0100 | 0.0256 |
| 4 | −0.0008 | 0.0080 | 0.0190 |
| 5 | −0.0005 | 0.0039 | 0.0132 |
| 6 | −0.0005 | 0.0026 | 0.0117 |
| 7 | −0.0005 | 0.0026 | 0.0117 |
| 8 | −0.0005 | 0.0026 | 0.0117 |
| 9 | −0.0005 | 0.0026 | 0.0117 |
| 10 | −0.0005 | 0.0026 | 0.0117 |

Table 3.3: Numerical solution for different values of $N$ when $x = 0.2$.

Due to the lack of closed-form solutions for bioheat transfer problems or experimental data, the current study uses the validation approach that was employed by earlier research (Kumar and Rai (2016), Li et al. (2020)). Hence, for the purpose of verification of the present numerical scheme, we consider the particular case when this coupled bio-thermoelastic model is simplified to a heat conduction problem based on a single layer of skin tissue. This particular problem is solved by applying the Laplace transform method to find the exact solution. The temperature distribution produced through the present scheme is therefore compared to the solution achieved by using the Laplace transform approach as displayed in Fig. 3.2.2. The temperature plot by both methods is seen to be in good agreement, indicating that the current numerical procedure is accurate and effective.

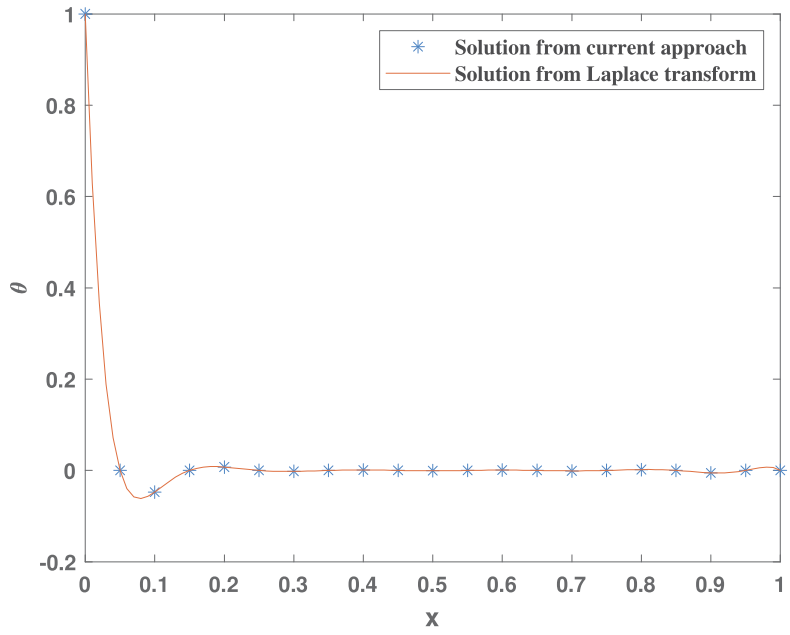


Figure 3.2.2: Comparison of temperature distribution obtained from different methods.

#### 3.2.7.2 Influence of variable thermal conductivity

Figs. 3.2.3-3.2.5 depict the effects of temperature dependency parameter of thermal conductivity on the distributions of displacement, temperature, and stress when $t = 0.1$, $\tau_{q1} = 0.01$ and $\tau_{q2} = 0.005$. From Fig. 3.2.3, it is observed that the displacement increases as the value of $\chi_1$ approaches a higher negative value, whereas temperature and stress decrease as the temperature dependency parameter $\chi_1$ decreases. This fact is very clear from Figs. 3.2.4 and 3.2.5. In other words, disregarding the variable thermal conductivity causes the temperature and stress to be enhanced. As it can be seen that the displacement and stress are strongly influenced by $\chi_1$, whereas the variable conductivity coefficient appears to have no significant effect on the propagation speed of heat response. However, variable thermal conductivity coefficient $\chi_2$ almost has no effect on thermoelastic responses in the region of normal tissue.

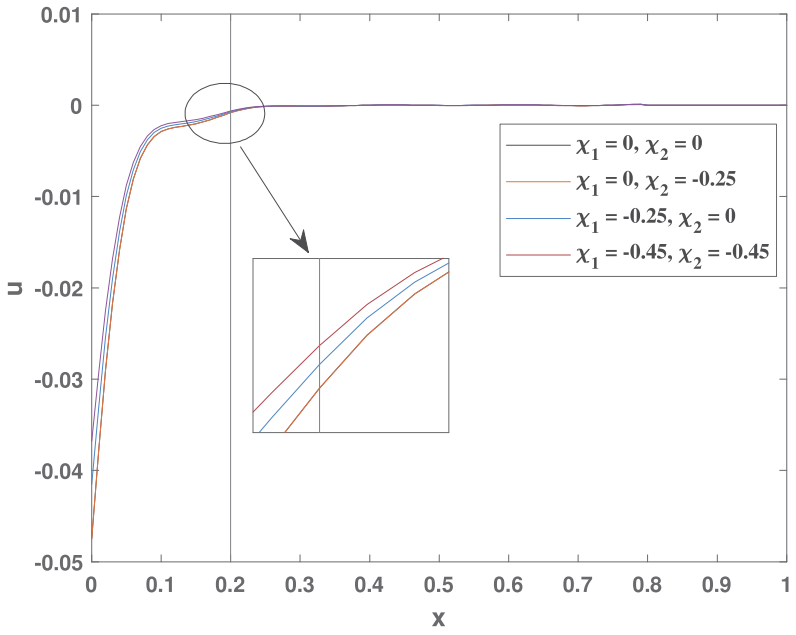


Figure 3.2.3: Influence of variable thermal conductivity on displacement distribution at $t = 0.1$.

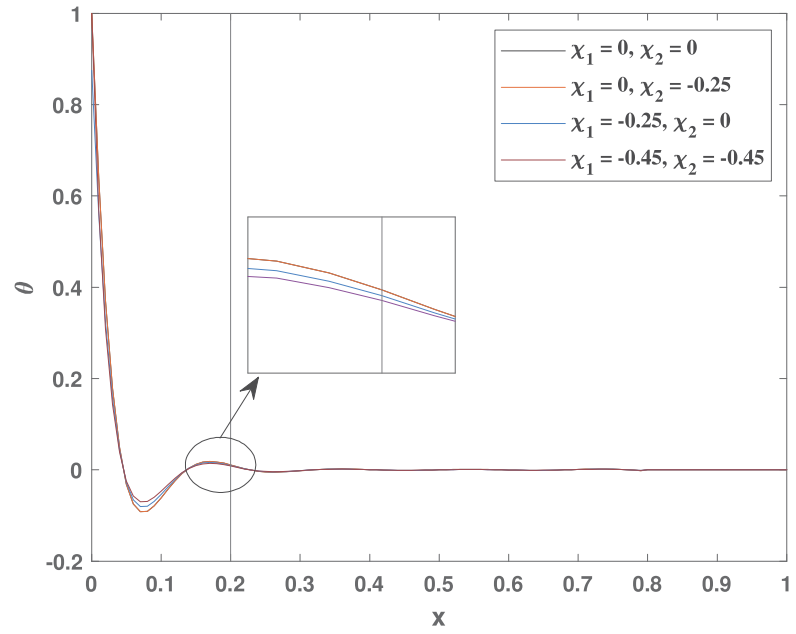


Figure 3.2.4: Influence of variable thermal conductivity on temperature distribution at $t = 0.1$

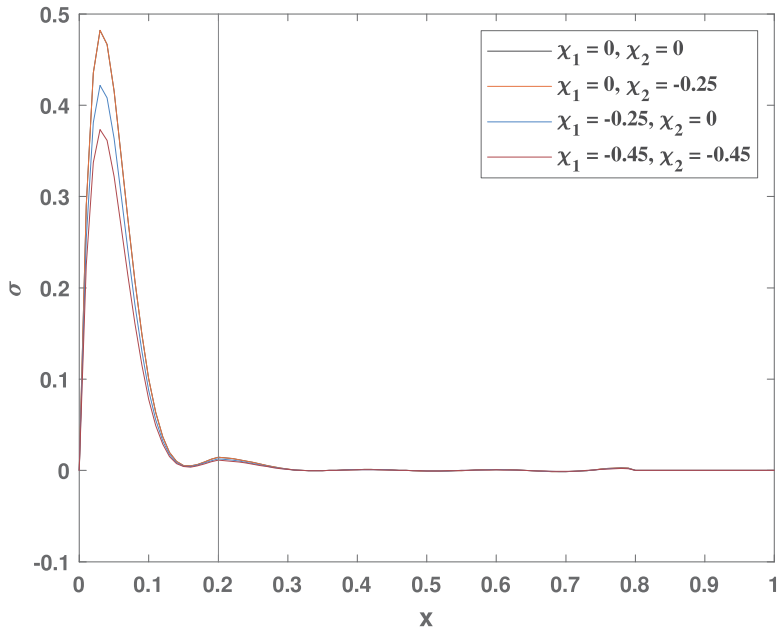


Figure 3.2.5: Influence of variable thermal conductivity on stress distribution at $t = 0.1$.

#### 3.2.7.3 Influence of thermal relaxation parameters

The effects of thermal relaxation parameters ($\tau_{q1}$, $\tau_{q2}$) on displacement, temperature, and stress for $\chi_1 = \chi_2 = -0.3$ and $t = 0.1$ are presented in Figs. 3.2.6-3.2.8. The impact of thermal relaxation parameters is similar to the case of variable thermal conductivity. As can be exhibited, the temperature is only little impacted by the thermal relaxation parameters while displacement and stress are significantly impacted. According to Fig. 3.2.6, the increment of ($\tau_{q1}$, $\tau_{q2}$) enhance the displacement. On the other hand, temperature and stress decrease with the increase in relaxation parameters, which is evident in Figs. 3.2.7 and 3.2.8. Furthermore, no disturbance is detected after the tumor-normal tissue interface position.

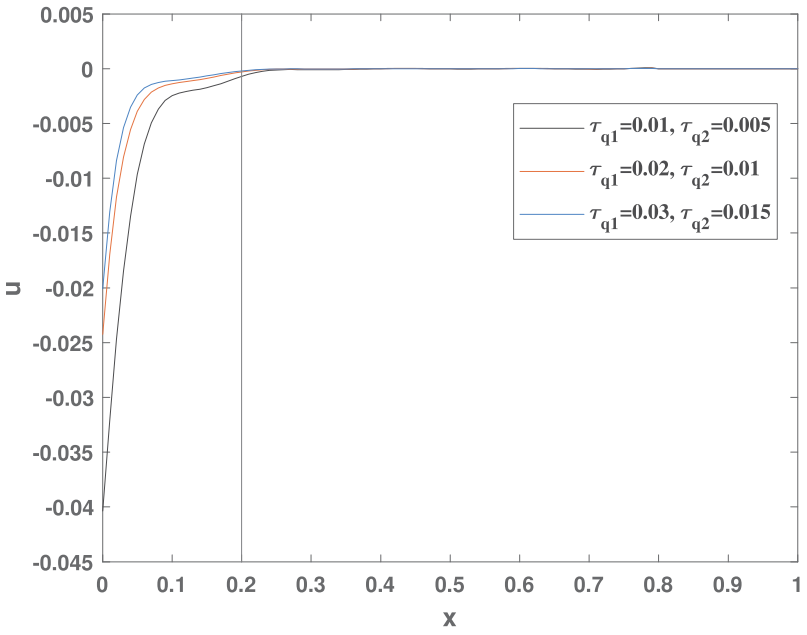


Figure 3.2.6: Influence of thermal relaxation parameters on displacement distribution at $t = 0.1$ and $\chi_1 = \chi_2 = -0.3$.

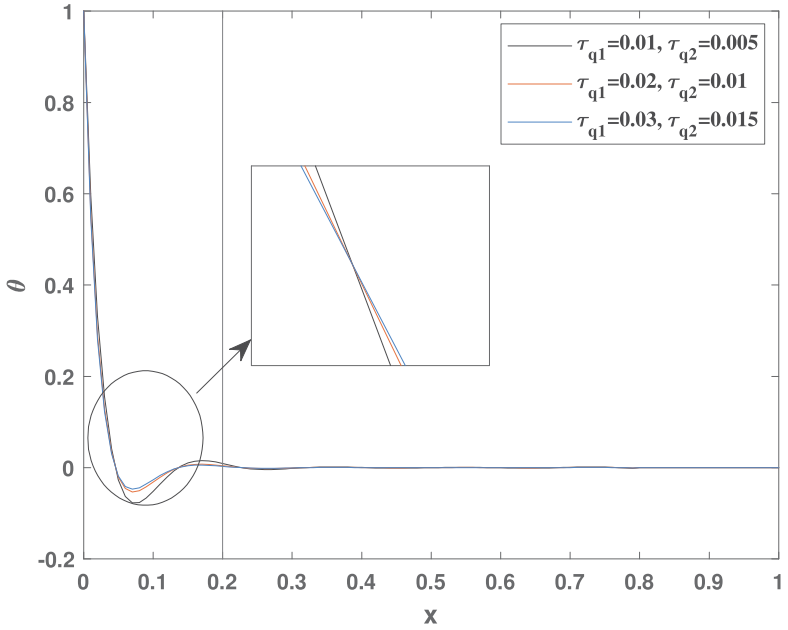


Figure 3.2.7: Influence of thermal relaxation parameters on temperature distribution at $t = 0.1$ and $\chi_1 = \chi_2 = -0.3$.

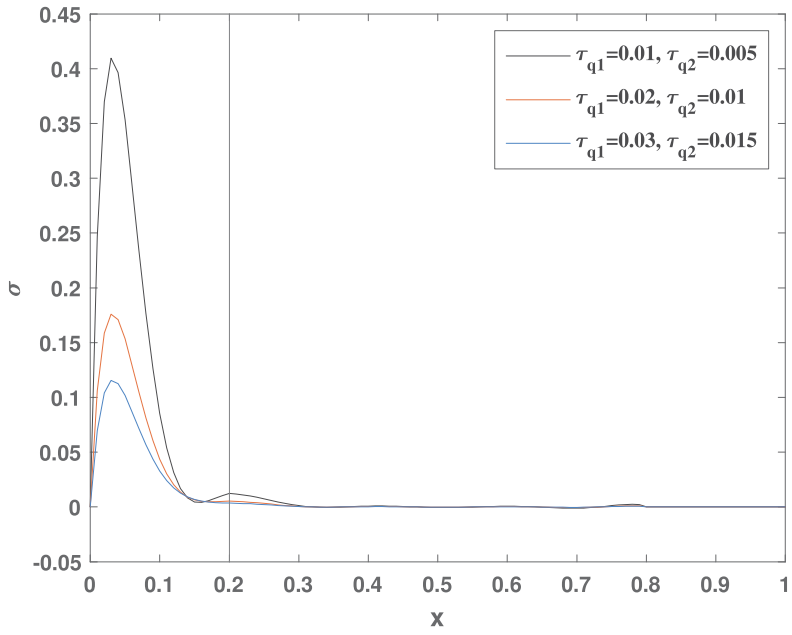


Figure 3.2.8: Influence of thermal relaxation parameters on stress distribution at $t = 0.1$ and $\chi_1 = \chi_2 = -0.3$.

#### 3.2.7.4 Responses at different instants of time

In this case, we look at the impacts of time $t$ on displacement, temperature, and stress. To display the effects of time, the distributions of field variables are shown at three distinct instants of time, i.e., at $t = 0.2, 0.3$ and $0.4$, while other parameters are specified as $\chi_i = -0.3\,(i = 1, 2)$, $\tau_{q1} = 0.01$ and $\tau_{q2} = 0.005$. From Figs. 3.2.9 and 3.2.11, it is apparent that as time $t$ increases the magnitude of displacement and stress increases. In addition, it is worth mentioning that time only has a visible impact on displacement and stress, whereas temperature is regarded to be independent of time. Hence, from these Figs. 3.2.9-3.2.11, we can conclude that the effective zone of influence expands over time for displacement and stress fields.

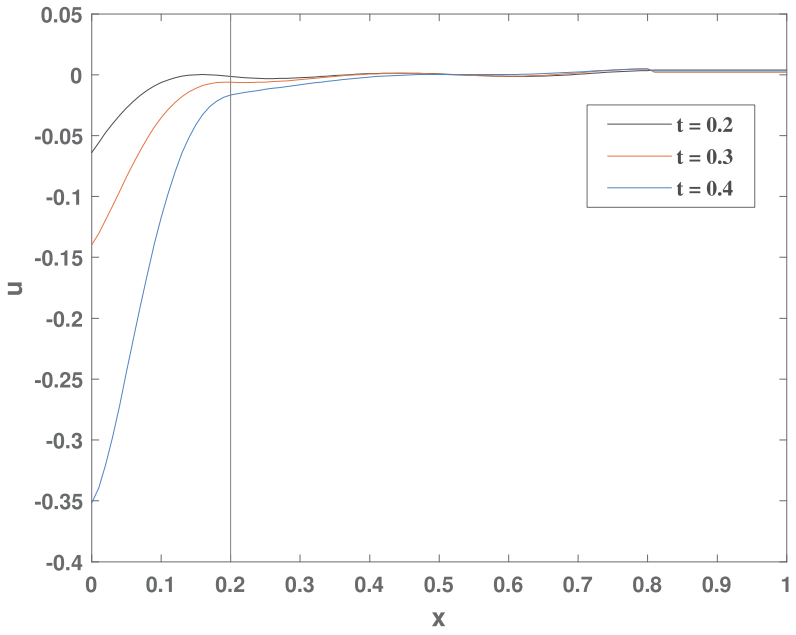


Figure 3.2.9: Displacement distribution at different instants for $\chi_1 = \chi_2 = -0.3$.

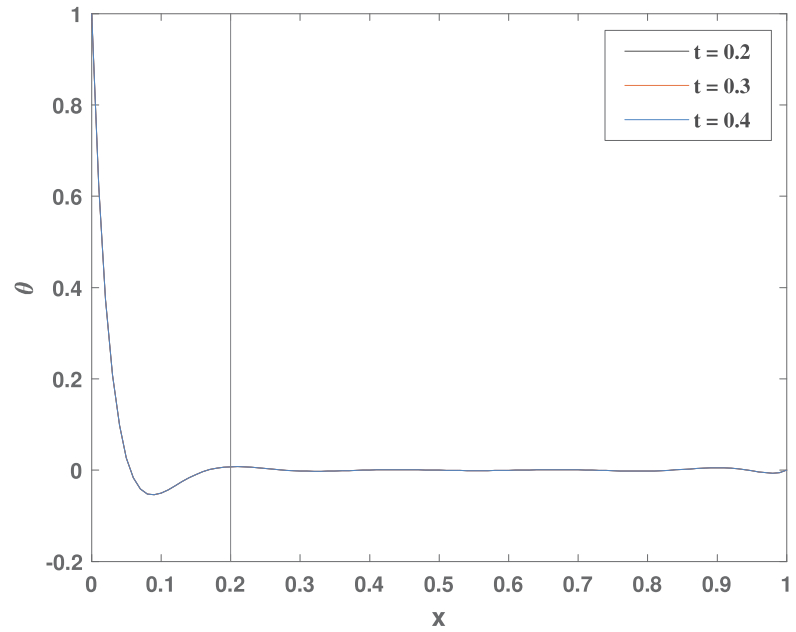


Figure 3.2.10: Temperature distribution at different instants for $\chi_1 = \chi_2 = -0.3$.

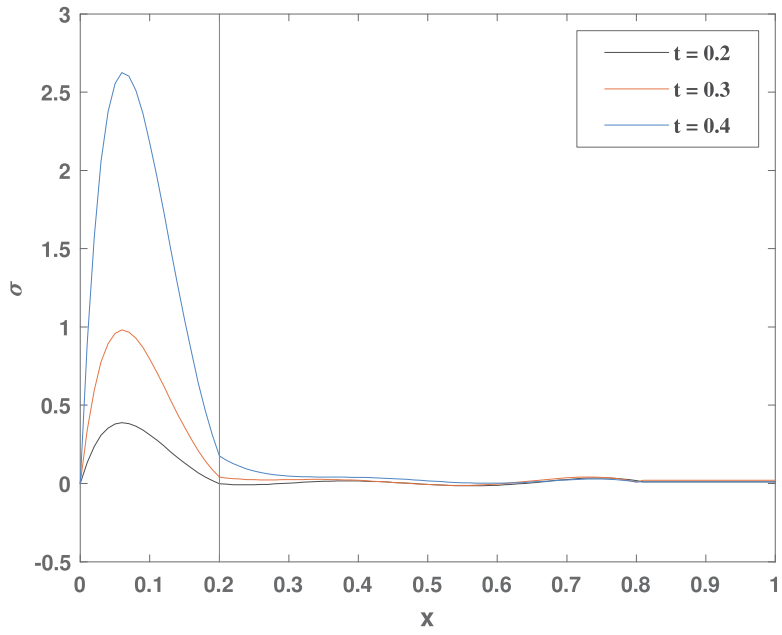


Figure 3.2.11: Stress distribution at different instants for $\chi_1 = \chi_2 = -0.3$.

#### 3.2.7.5 Comparison between different models

Now, we pay attention to the comparison among the predictions of different thermoelastic models such as Biot, LS, GN-III, and MGT models when $t = 0.1$ and $\chi_i = -0.3\,(i = 1, 2)$. The classical thermoelastic model (Biot model) can be obtained by assigning $\tau_{qi} = K^*_{i0} = 0\ (i = 1, 2)$. The LS model will be acquired by assuming $K^*_{i0} = 0$. For the GN-III model, $\tau_{qi} = 0$ is considered and in case of the MGT model, $\tau_{qi}$, $K^*_{i0}$ are non-zero. Figs. 3.2.12-3.2.14 exhibit that the thermoelastic responses in the affected zone for the Biot and GN-III models are higher than those for the LS and MGT models. It is worthy of attention in these figures that the results of the MGT model match very closely with the LS model. On the contrary, the profiles for the Biot and GN-III models match together. Clearly from the figures, the nature of all of the field variables is similar, with just minor variances in magnitude. Thus, the parameters $\tau_{qi}$ and $K^*_{i0}$ $(i = 1, 2)$ have significant impacts on thermal and elastic reactions in biological tissue.

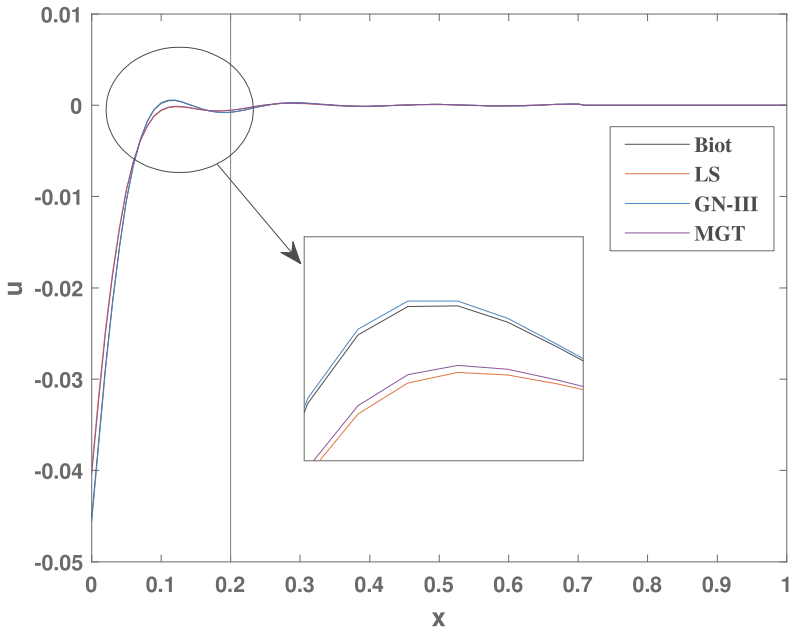


Figure 3.2.12: Displacement distribution for different models at $\chi_1 = \chi_2 = -0.3$ and $t = 0.1$.

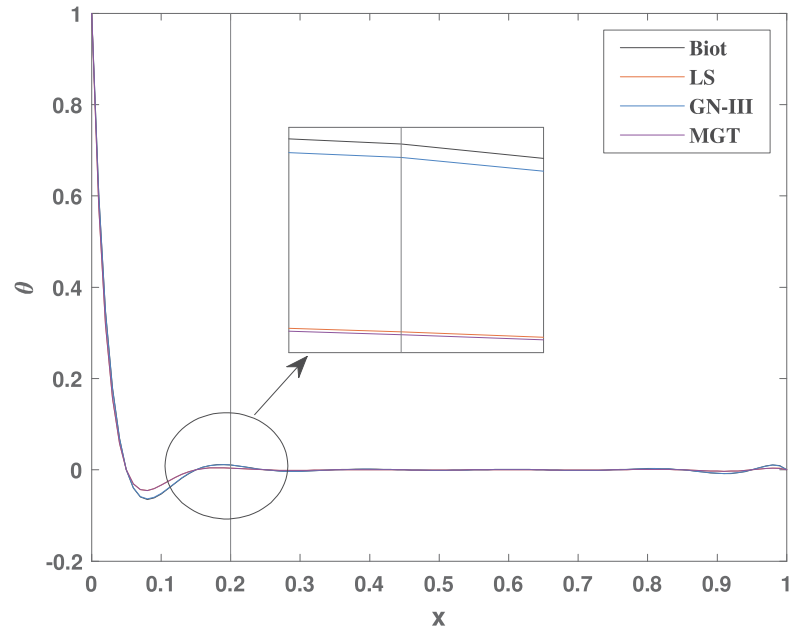


Figure 3.2.13: Temperature distribution for different models at $\chi_1 = \chi_2 = -0.3$ and $t = 0.1$.

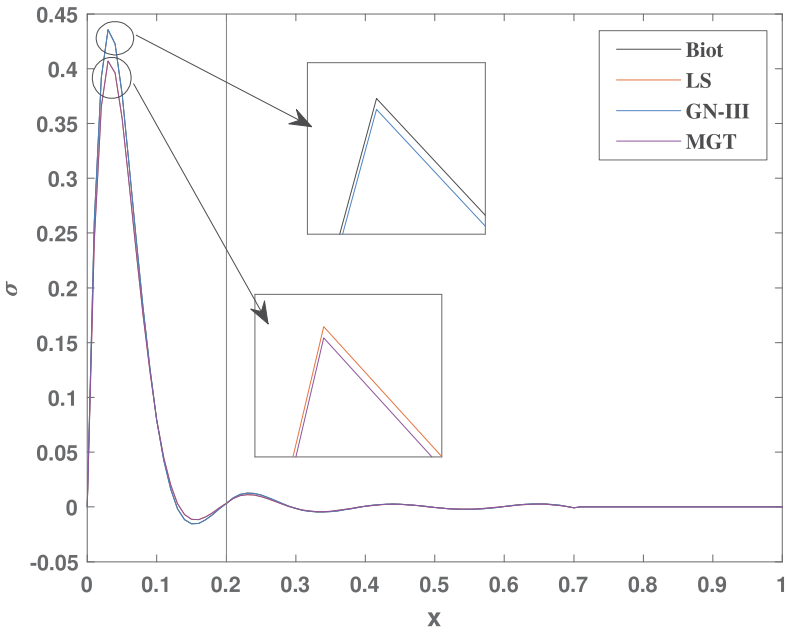


Figure 3.2.14: Stress distribution for different models at $\chi_1 = \chi_2 = -0.3$ and $t = 0.1$.

### 3.2.8 Conclusion

This study examines the thermal and mechanical responses in the tumor and normal tissues during laser irradiation within the bioheat transfer model based on Moore-Gibson-Thompson (MGT) heat conduction. Material characteristic like variable thermal conductivity is taken into account in the present problem. To solve the coupled equations with boundary and tumor-normal tissues interface conditions, we implement the Legendre wavelet collocation approach. Impacts of the variable thermal conductivity and relaxation parameters on displacement, temperature, and stress distributions have been studied in depth and a comparison between the MGT thermoelasticity and previous generalized thermoelastic models is made. The following significant key facts of the present investigation can be categorized:

- The main accomplishment of the current study is the proposal of an alternative numerical approach based on Legendre wavelet collocation that is capable of exploring thermoelastic responses in any coupled bio-thermoelastic problem ade-

quately like the finite difference method, finite element method, integral transform method, etc.

- Despite using a simpler framework and fewer collocation points, the present method provides satisfactory outcomes.

- The influence of variable thermal conductivity on biological tissue, particularly on tumor tissue, is essential to their thermoelastic response. The temperature and stress in tumor tissue will be overestimated if the temperature-dependent thermal conductivity is ignored. In other words, if the thermal conductivity remains constant throughout thermal therapy, the desired impact may not be attained. Unlike the case of tumor tissue, variable conductivity coefficient $\chi_2$ almost has no effect on all responses in normal tissue.

- During laser irradiation, the thermal relaxation parameters considerably influence the transient responses. The displacement, temperature and stress decrease with an increase in thermal relaxation parameters, while the displacement has the opposite effect.

- Despite the graphs indicate similar results for all the models, there are some discrepancies between the results that the magnitude is greater for the Biot and GN-III models than the MGT and LS models. Moreover, the LS and MGT models both make predictions that are in agreement.

- All of the field variables exhibit non-zero values only inside a bounded region and vanish outside of the tumor-tissue interface point, demonstrating the finite speed of thermoelastic wave propagation by the present thermoelastic model.

- It is worth noting here that the effective region of influence for the theory of classical thermoelasticity is shown to be greater because it exhibits infinite speed

behavior as opposed to the MGT model, which allows for finite speed of heat signals.